

**BREAKING THE LIMIT FOR BIO-SENSING:
SENSITIVITY ENHANCEMENT OF RESONANT CAVITY DUE TO SUB-
WAVELENGTH CONFINEMENT BY HETEROGENEOUS DIELECTRIC
LAYERING**

THESIS

for the Degree of

**BACHELOR OF SCIENCE
(Electrical Engineering)**

OPHIR GAATHON

MAY 2006

**Breaking the Limit for Bio-Sensing:
Sensitivity Enhancement of Resonant Cavity Due To Sub-Wavelength
Confinement by Heterogeneous Dielectric Layering**

T h e s i s

Submitted in partial fulfillment of the REQUIREMENT for the Degree of

BACHELOR OF SCIENCE (Electrical Engineering)

At the

Polytechnic University

By

Ophir Gaathon

May 2006

Approved:

Advisor, Stephen Arnold

_____2006

Department Head

_____2006

Copy No. _____

What is science?

“The exact sciences start from the assumption that in the end it will always be possible to understand nature, ... but that we may make no a priori assumption as to the meaning of ‘understand’.”

Werner Heisenberg

VITA

Mr. Ophir Gaathon was born in St. Louis, Missouri on February 1st 1978. He completed his secondary studies at Ziv & Marx High School in Jerusalem Israel – the country where he grew up. After serving for three years in the Engineering Corps of the Israeli Defense Force Ophir moved to the United States. In New York he worked for two and a half years in a broadcast design company as a production artist. In September 2002 Ophir started his undergraduate studies at Polytechnic University in Brooklyn. In the spring of 2004 he joined the Microparticle Photophysics Laboratory (MP³L). Under the guidance of Professor Stephen Arnold, Ophir focused his effort in finding a mean of enhancing the Whispering Gallery Mode sensor.

To my parents

ACKNOWLEDGMENT

I would like to thank my advisor Professor Stephen Arnold for introducing an amazing world to me in a way that taught me so much along the way. With his heuristic approach I got to discover the beauty and elegance in physics and nature. His continual support and motivation helped me push through the challenging times of research.

To Professor Teraoka thank you for our fruitful discussions about both theory and experiments. Special thanks to Professor Charles Martucci for his patience, dedication and encouragement. Thanks to Steve Holler for the open discussions and support. Also, I would like to thank Professor Henry Du and his student Wang-Chieh Yu at *Stevens Institute of Technology* for helping me with the SEM images.

I would like to thank Professor Neil Wotherspoon for taking the time to teach me lab electronics and machining. To my colleagues, the MP3L students: David, Ravi, Momchil & Jelena. Thank you for the collaboration, support and for your team spirit. Also, I would like to thank the lab's former PhD student, Mayumi Noto, which taught me the basics of surface chemistry and guided me through my first steps in the WGM sensing business.

To my department, Electrical Engineering, thank you for letting me take this less traveled path.

Abstract

**Breaking the Limit for Bio-Sensing:
Sensitivity Enhancement of Resonant Cavity Due To Sub-
Wavelength Confinement by Heterogeneous Dielectric Layering**

Ophir Gaathon

The whispering gallery mode (WGM) bio-sensor marries electromagnetics and photonics with biology and returns very high sensitivity. It accomplishes this by utilizing high quality factor resonator ($Q \sim 10^7$) in a mode in which adsorption by bio-molecules on its surface shifts the whispering gallery modes in the frequency domain. Its potential uses are expansive into many domains such as clinical assay and the assessment of bio-chemical threats, to name a few. As a consequence this area of research has seen exponential growth in the last few years. However it is not single-molecule sensitive; it falls short in its native state by about two orders of magnitude. Herein we present a dielectric design for a resonator in which light is squeezed into a small volume as it circumnavigates a silica microsphere. This is accomplished by adding a high refractive index sub-wavelength layer to the surface. The result is a theoretical enhancement in sensitivity of between one and two orders of magnitude.

The new dielectric structure had been fabricated by nano-layering on a silica sphere and introducing it into an evanescent coupling system. The demonstrated enhancement in sensitivity is 2.5X the published standard¹.

Table of Contents

Chapter	Page
Introduction	1
Chapter 1 - General Principles for Whispering Gallery Mode Sensors	3
Chapter 2 - Looking for Enhancement - Theoretical Framework	7
Chapter 3 – Experimental Results	15
– 3.1 Making the polystyrene coated spheres	15
– 3.2 Experimental setup	18
– 3.3 Protein adsorption – BSA	19
– 3.4 Index of refraction detection	22
Conclusion	24
References	25
Appendix	27
A- Complete derivation of the balloon quantum analog	28
B- Experimental protocols and technical information	43
C- Mathematica scripts	44
D- Manuscript - Spectroscopy Of Photonic Atoms: A Means For Ultra-Sensitive Specific Sensing Of Bio-Molecules	57

Figures and Graphs

Figure	Description	Page
1.1	Whispering gallery mode (WGM) ray diagram.	3
1.2	Whispering gallery mode (WGM) wave representations.	3
1.3	Potential diagram of solid sphere.	5
1.4	A protein molecule at position r_i on the surface of a sphere.	6
2.1	Potential diagram for a balloon.	9
2.2	Field distribution for two well widths.	9
2.3	Intensity distributions near the skin of μ -balloons having different thicknesses.	10
2.4	Enhancement curves of the balloon in air and water with the corresponding evanescent field lengths.	12
2.5	Enhancement curve of polystyrene in air with asymptotes	13
3.1	Dipped sphere	15
3.2	Anchoring di-phenyl-methyl-chloro-silane to silica	16
3.3	SEM & AFM images of polystyrene scratched layer	17
3.4	Experimental setup	19
3.5	BSA adsorption illustration	20
3.6	Resonance shift due to BSA adsorption data	20
3.7	Spectrum change while BSA adsorbs to the polystyrene surface	21
3.8	Fractional resonance shift due to NaCl addition	22
A.1	Potential diagram for a balloon.	32
A.2	The different components of vector k inside the layer (top view).	33

Introduction

One of the most basic processes in our bodies is the interaction between macromolecules (such as protein-protein and DNA-protein). Examples of these interactions are illustrated by our ability to replicate DNA, silence genes, or identify infectious agents (e.g. viruses and bacteria) through antibodies. Understanding the kinetics involved in these types of interactions are critical for the development of new drugs for diseases such as cancer and Alzheimer. In addition, with the growing concern for biological / chemical terrorism there is a need for fast and reliable sensors that can detect minute concentrations of agents in the early stages of an attack. To do so, an ultrasensitive and highly specific sensor must be developed.

The use of resonant spherical optical microcavities as sensors has been a subject of intense research for several years. The detection scheme utilizes the interaction between photons that are trapped inside a microsphere and molecules on its surface. As light is confined by total internal reflection inside the sphere, a rapidly decaying evanescent field exists at the surface. This evanescent field polarizes the molecules which in turn causes a shift in the resonance frequency. In order to make this interaction specific one can exploit nature's highly selective bio-interactions. By functionalizing the surface of the microspheres to compliment a target body (protein, Virus, DNA, etc.) the selective biosensor was born¹.

Due to the special geometry and other properties of silica microspheres the characteristic line-width is very narrow (~ 1 part in 10^8 in frequency). This enables us to notice subtle changes in frequency.

But unfortunately we face an experimental obstacle. In the attempt to sense an infinitesimally small number of molecules (with the final goal of a single molecule) we have

to pass a noise barrier. The signal to noise ratio is simply too small. Even though, in principle, the possible sensitivity of the optical system can be down to a single molecule, experimental constraints (such as electronic noise and thermal fluctuations) prohibit us from reaching that limit.

Ideally, we would like to amplify the shift from our optical system. As this detection scheme is intensity independent (pumping more light into the system does not increase sensitivity) we need to be able to change the strength of the interaction between the evanescent field and the molecules. In other words, our goal is to make the sensing of every molecule more dramatic. Here we propose a method to push light to the surface of the sphere by confining it to a thin film around the sphere. By forcing light to travel closer to the surface we in effect redistribute the wave, exposing more of it evanescently to the outside.

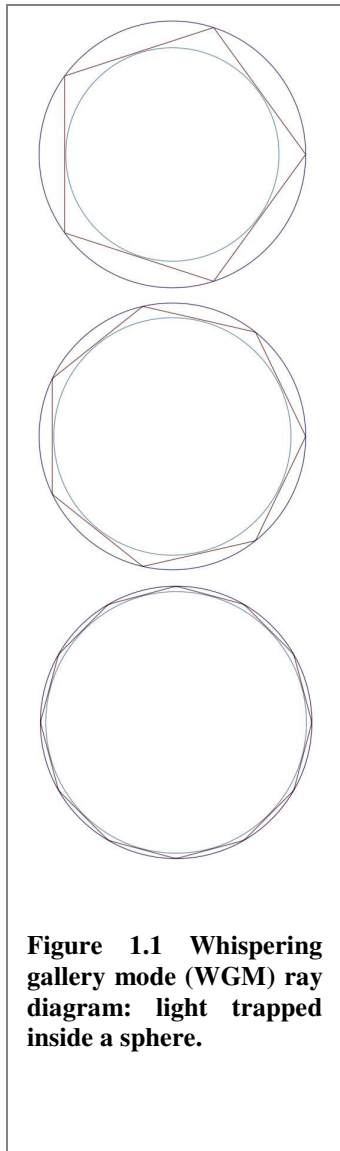
In the next chapter (chapter 1) we will cover the basic theoretical principles for the standard whispering gallery mode sensor. These principles serve as the foundation upon which we will build the framework for enhancement (chapter 2). In chapter 3 we will cover the preliminary experimental results that demonstrate this enhancement. Finally, at the end of the thesis there are several appendices that complement the chapters and provide more detailed information that unfortunately could not be put into the chapters without digressing.

A short note about the heuristic approach taken in this thesis:

There are many ways to model how light is confined inside a microsphere. Ray optics and electromagnetic waves are some of the most common methods; each one has its own advantages and deficiencies. The motivation behind modeling is to help us understand how things work. Insight is what should drive a model. Ray optics for example can provide, a more visual way of seeing how light bounces from the inner surface of the sphere in what are called Whispering Gallery Modes². However, the ray optics picture does not contain phase information and cannot easily explain evanescent fields. By solving Maxwell equations and matching boundary conditions for this system we can have a solution that is the most precise. Unfortunately this analysis is quite rigorous and computationally laborious. At the Microparticle Photophysics Laboratory we are used to visualizing the system using a quantum analog to Bohr's Atom^{3,4}. This enables us to reduce the complexity of the system down to tangible elements that enrich our understanding.

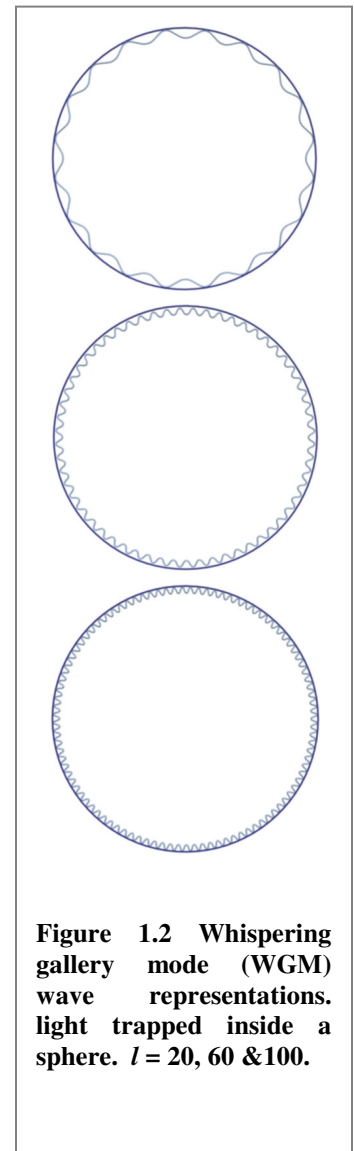
Chapter 1

General Principles for Whispering Gallery Mode Sensors



Imagine a continuous stream of light (photons) that is being injected into a microsphere. Inside the sphere, along the equator, the light skips along the sphere's boundary by total internal reflection (figure 1.1).

As the light returns after completely circumnavigating the sphere it will be either in or out of phase with the continually injected stream. Looking at light as a wave (figure 1.2) we can say that the wave orbiting the sphere interfere with the wave entering the sphere. If the waves come together when they are out of phase, the circulating energy will be attenuated. But if the waves meet in phase we get constructive interference and the resulting wave is stronger. Because the photons are



trapped in the sphere for much longer than one orbit, there is a buildup of intensity for those wavelengths that are in phase. That is: only wavelengths that make an integer number of cycles in a trip are optimally sustained.

This might be a good point to introduce the term: quality factor Q. As described above, photons may be trapped inside the sphere for many passes (~1,000,000 times) before they leak out. Clearly the more orbits the photons make before it escapes the more selective the sphere is. The Q is linearly proportional to the life time of the photon in the sphere. Accordingly, only certain wavelengths (or frequencies) can bring the sphere into resonance. As the sphere radius changes the resonance frequency changes.

However, there is more to the story. When photons skips along the inner boundary of the sphere an evanescent field is generated outside. One way of visualizing this phenomenon can be made through a quantum analog.

The quantum analog for photon confinement is constructed as follows. By representing the electric field in terms of a scalar function $\mathbf{E} = \hat{L}\Psi$, where \hat{L} is a dimensionless angular momentum operator. The problem of solving the vector wave equation is easily reduced to the solution of a Schrödinger-like equation for the radial part of Ψ ; ψ_r ⁶. The effective energy E_{eff} for this quantum analog is the square of the free space wave vector, $E_{\text{eff}} = k_0^2$, and the effective potential

$$V_{\text{eff}} = k_0^2 (1 - n(r)^2) + \ell(\ell + 1) / r^2 \quad (1.1)$$

where $n(r)$ is the radial refractive index profile, and ℓ is the angular momentum quantum number of a particular mode. The use of the quantum analog allows for simplifications which enable one to obtain physical insights. See Figure 1.3.

From the figure one can see that the potential V falls for $r < R$. The step in the potential $r = R$ is attributed to the change in the index of refraction as r becomes larger then the radius of the sphere R. The characteristic length of the evanescent field at grazing incidence is given by⁵

$$l_{es} \approx \frac{1}{2k_0(n_{\text{eff}}^2 - n_m^2)^{1/2}}, \quad (1.2)$$

where n_{eff} and n_m are the refractive indices of the resonant mode, and the external medium, respectively.

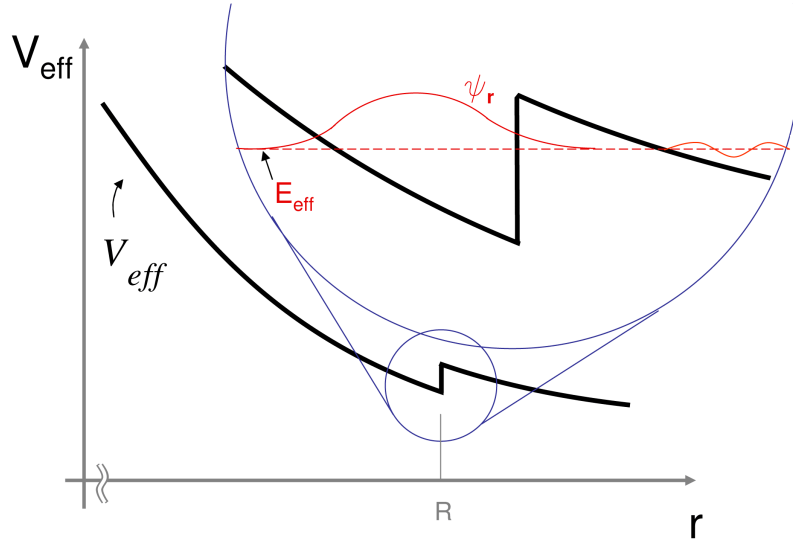


Figure 1.3 – potential diagram of solid sphere. Insert shows the first mode of the wave function, where the evanescent field extending in to the classically forbidden regions.

A typical length is on the order of about 100nm. The origin of the field in the potential diagram is seen beyond the classical turning point in figure 1.3. Unlike a flat interface in which there is no dissipation outward, in the case of the sphere the energy level emerges through the potential barrier (see insert, figure 1.3). Photons are generated leading to dissipation. Since this point is usually a couple of microns from the surface a nanometer-size bio-particle is bathed in the evanescence portion of the field. The field E_0 polarizes the particle, which leads to a perturbation in the frequency of the mode. The relative frequency shift for a single particle positioned at \mathbf{r}_i and interacting with the resonant sphere can be described by⁶

$$\frac{\delta\omega}{\omega} = \frac{-\alpha|\mathbf{E}_0(\mathbf{r}_i)|^2}{2\int\epsilon(\mathbf{r})|\mathbf{E}_0(\mathbf{r})|^2 dV}, \quad (1.3)$$

where α is the polarizability of the particle, and $\epsilon(\mathbf{r})$ is the dielectric function throughout space. The strength of the interaction is proportional to the relative strength of the field on the surface compared to the total field.

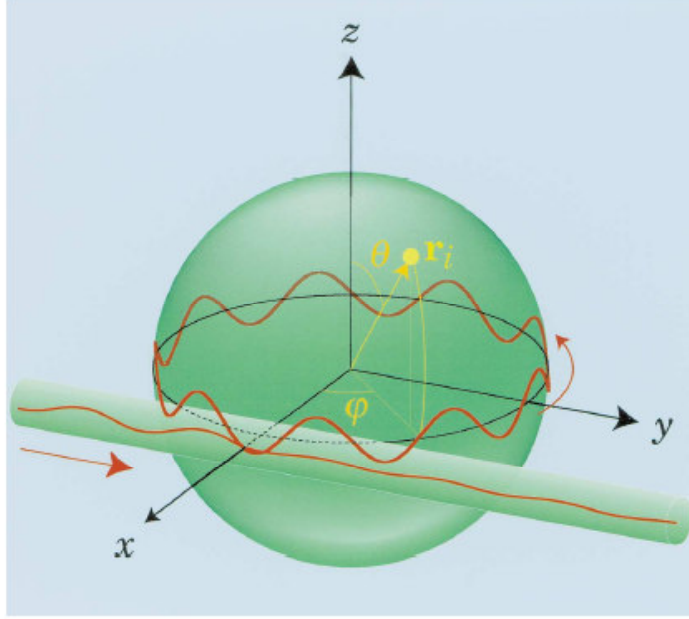


Fig. 1.4 A protein molecule at position r_i on the surface of a sphere near an eroded optical fiber core ⁶.

For a single particle landing on the sphere at position (R, θ, ϕ) and interacting with a photon orbiting the equator, Eq.1.3 can be evaluated to be approximately⁶,

$$\left(\frac{\delta\omega}{\omega}\right)_{Solid} \approx \frac{-\alpha|Y_{ll}(\theta, \phi)|^2}{\epsilon_0(n_s^2 - n_m^2)R^3}. \quad (1.4)$$

Where Y_{ll} is the spherical harmonic describing the angular part of the spherical wave function, ϵ_0 is the permittivity of free space, n_s and n_m are the indices of refraction of the sphere and medium respectively.

Eq.1.4 describes what is currently the most sensitive unlabelled detection paradigm, but it is not currently “single molecule sensitive.” Until now experiments have been carried out using a random statistical number of molecules on the surface, and the shift has been evaluated by integrating Eq.1.3 over random surface positions. In the next chapter we will outline a scheme for further increasing the sensitivity, by utilizing a heterogeneous dielectric function (i.e. not just a solid homogenous sphere).

Chapter 2

Looking for Enhancement

In the previous chapter we discussed the case of a solid sphere that is brought into resonance. Here we will concentrate on how we can enhance the sensitivity of the whispering gallery mode sensor. As mentioned before, the magnitude of the frequency shift is controlled by the strength of the interaction between the molecule and the field at the surface. Obviously, we cannot change the polarizability of the analyte at hand, but we can change the field strength at the surface. Looking at Eq. 1.3 we can extract a ratio that would serve as a measure of the strength of the field. One can see that this optical ratio R_{opt} does not depend on the analyte.

$$R_{opt} = \frac{-1}{\alpha} \frac{\partial \omega}{\omega} = \frac{|\mathbf{E}_0(\mathbf{r}_i)|^2}{2 \int \epsilon(\mathbf{r}) |\mathbf{E}_0(\mathbf{r})|^2 dV} \quad (2.1)$$

To optimize R_{opt} we attempt to maximize optical confinement near the surface. This is most easily accomplished by utilizing the tendency for a high refractive index material to attract light. By drawing more energy toward the surface we increase the field in the numerator of Eq. 2.1 relative to the energy in the denominator, and thereby increase R_{opt} . A practical system would be a high index layer on a glass substrate. A high index balloon represents a simpler structure. The way in which the balloon optics enhances bio-sensing (i.e. R_{opt}) may be understood best by going back to the quantum analog.

Figure 2.1 illustrates the radial part of the potential diagram of a balloon mentioned in Eq.1.1. The ‘fracture’ in the centripetal potential at R represents the contribution of the balloon skin index enabling a local minimum. By viewing the magnified insert of this notch of width t , one can hardly resist thinking of this problem as one of confinement in a finite potential well centered at $r = R$. With this inspiration we shift our attention to this well

through the coordinated transformation $\xi = r - R$. The propagation constant in the skin $n_{Layer} k_0$ is composed of two components; a radial component k_ξ and a tangential component k_ϕ ; $(n_{Layer} k_0)^2 = k_\xi^2 + k_\phi^2$. The angular momentum quantization of the orbiting photon constrains k_ϕ ; $k_\phi^2 = l(l+1)/R^2$. Beyond this k_ξ may be evaluated approximately by considering it to be the result of motion in a finite potential well of depth $k_0^2 (n_{Layer}^2 - n_{Out}^2)$ where n_{Layer} and n_{Out} are the refractive indices of the layer and the medium outside, respectively. We can define a relative index as the ratio of the two; $n_{relative} = n_{Layer}/n_{out}$. This ratio that folds in to it all the refractive index parameters is the measure of contrast between the layer and its surroundings. As stated before the field confinement depends on that contrast. This problem requires matching boundary conditions from which k_ξ may be found from the transcendental equation (see appendix A equation A.51),

$$\tan(z) = \frac{1}{n_{relative}} \sqrt{(z_{max}/z)^2 - 1} \quad (2.2)$$

where $z = k_\xi t/2$, and z_{max} is the value of z as the effective energy climbs to the top of the potential well.

$$z_{max}^2 = k_\phi^2 \left(\frac{t}{2} \right)^2 (n_{Relative}^2 - 1) \quad (2.3)$$

the result for z from equation 2.2 defines the effective energy (equation A.34 in the appendix) and the wavefunction, (equations A.41 and A.45) as illustrated in the insert in figure 2.1.

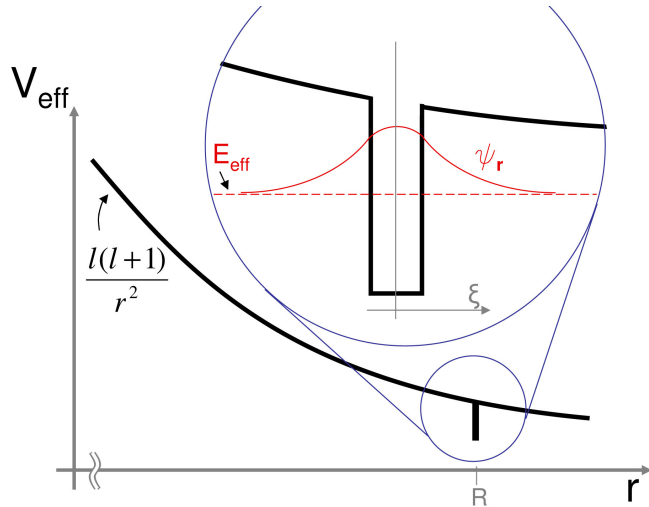


Fig. 2.1 Effective potential vs. radial distance for a spherical balloon 100 μm in radius and having a wall thickness t . The balloon of refractive index n is filled with and surrounded by air.

As one can see the photon has considerable probability of being found in the classically forbidden regions (i.e. beyond the boundary of the well). The effect of reducing the width of the well is shown in figure 2.2.

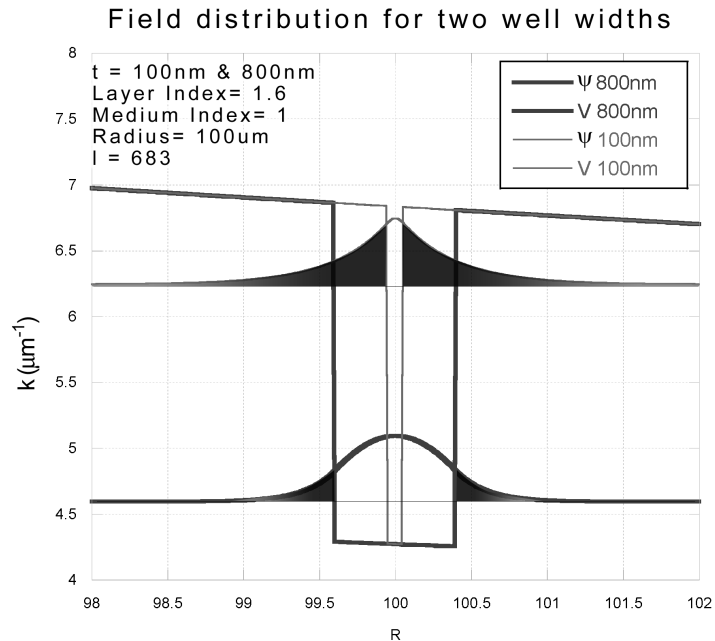


Fig 2.2 Field distribution for two well widths. The shaded area represents the evanescent field as it extends beyond the well boundary.

The single change in well width, from 800nm to 100nm, in the figure produces two kinds of changes. First the effective energy is increased, and second, the probability of

finding a photon outside the well is preferred. Both of these tendencies are persistently followed with shrinking the width as illustrated by figure 2.3. The pronounced spread in the wavefunction at 25nm is reminiscent of a slow exponential decay as the effective energy approach the top of the well. Recall the Quantum-Analog Schrödinger equation

$$\psi'' = -[\mathcal{E}_{eff} - V_{eff}] \psi, \quad (2.4)$$

it is apparent that as \mathcal{E}_{eff} approach V_{eff} the coefficient on the right moves toward zero, and the solution $\sim e^{-[\mathcal{E}_{eff} - V_{eff}]^{1/2} \xi}$; a slow decay should be evident.

It should be noted that the “ground state” cannot be pushed out of the well by reduction in width. This is a characteristic of the finite potential well. At most one can push the state closer to the top by reducing the width, however its ground state remains for any width. This sort of effect falls in to the realm of a new area of research known as nano-optics. Layers such as those which will yield our best bio-sensor sensitivity will be “sub-wavelength”.

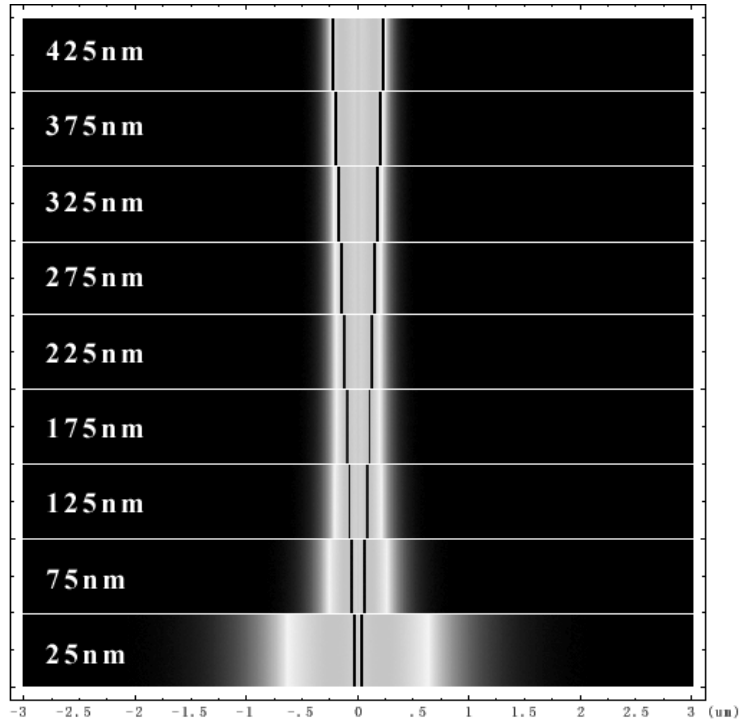


Figure 2.3 Intensity distributions near the skin of μ -balloons having different thicknesses. A particle landing on the surface of a thinner layer would be subject to a much greater field causing it to be more strongly polarized and subsequently promoting a larger shift of resonance frequency. (Parameters: $n_{Layer} = 1.6$, $n_{Out} = 1$, $R = 100\mu m$, $l=683$).

However, an undesirable effect gradually emerges as we look for enhancement from the layer. Looking back at Eq. 2.1, one can see that even though the field at the boundary increases (the numerator), the integral over the volume in the denominator increases even more, which pulls the ratio down. In conclusion, the greatest ratio would be somewhere between the two extremes.

In order to compute equation 2.1 for the balloon configuration one can divide the integral in the denominator in to its three parts (inside the balloon, in the layer and outside) and evaluate each separately with the proper index of refraction. Considering that the integral over the spherical harmonic in the denominator is 1, the resulting shift is given by,

$$\left(\frac{\partial \omega}{\omega}\right)_{Layer} = \frac{-\alpha |Y_{ll}|^2 / R^2}{\epsilon_0 n_{Layer}^2 t \left[\sec^2(z) + \frac{\tan(z)}{z} \right] + 2\epsilon_0 n_{Out}^2 l_e} \quad (2.5)$$

(note that details of the derivation of equation 2.5 can be found in the appendix, equation A.65)

Equation 2.5 provides a great deal of physical insight into the major components that affect the resonance shift. Focusing on the denominator, one can see that there are two major components to it. The first is associated directly with the layer thickness while the second is related to the characteristic length of the evanescent field. The factor of two in the second term is due to the integration of the two evanescent field regions to the sides of the layer (i.e. inside and outside the balloon).

To evaluate the enhancement of the shifts for the micro-balloon above that of the solid sphere of the same size, requires only that we divide equation 2.5 by equation 1.4;

$$\mathcal{E} = \frac{\left(\frac{\partial \omega}{\omega}\right)_{Layer}}{\left(\frac{\partial \omega}{\omega}\right)_{Solid}} = \frac{(n_{Layer}^2 - n_{Out}^2)R}{n_{Layer}^2 t \left[\sec^2 z + \frac{\tan z}{z} \right] + 2n_{Out}^2 l_e} \quad (2.6)$$

where ($n_m = n_{Out}$). We can use this equation to scan through different layer thicknesses to see which would most enhance the shift. Figure 2.4 shows the enhancement curves of the balloon in air and water.

Looking at the figure one can see that the optimal enhancement for the balloon in water occurs for a larger layer thickness in comparison with a balloon surrounded by air. In addition, the enhancement in water although significant, is considerably smaller. This is understandable since the reduced dielectric contrast in water leads to a correspondingly reduced confinement. Such intuitive notions are more readily obtained by avoiding the transcendental equation (Eq 2.2). Indeed, approximate analytical solution can be obtained for asymptotic limits.

We wish to be able to obtain a physical understanding that would enable us to estimate at what film thickness the enhancement (Eq. 2.7) is optimal. One can see that the numerator remains constant while varying the film thickness. On the other hand, each of the two portions of the denominator varies significantly for different layer thickness. This competing relationship builds up to asymptotes that would guide us in this respect. A linear approximation can be made to the evanescent length for small t/l_e , $l_e^{-1} \approx k_\phi^2(n_{relative}^2 - 1)t/2$. This can be utilized to construct an asymptotic equation for the enhancement in this range. On the other hand, at large t/l_e the enhancement is controlled by

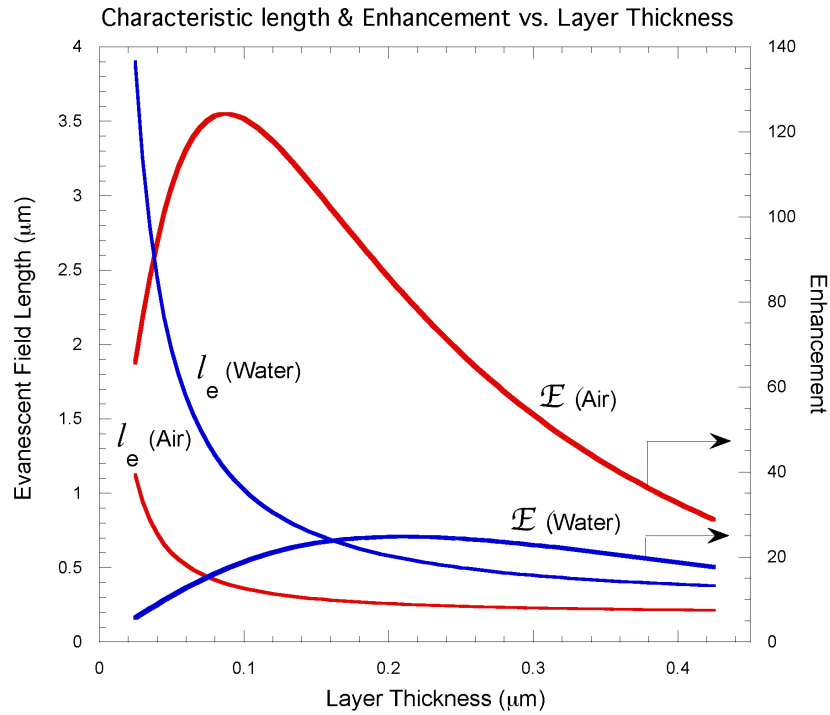


Figure 2.4 Enhancement curves of the balloon in air and water with the corresponding evanescent field lengths.

the first term in the denominator as such an asymptote can be constructed so that, with the appropriate constants, one can use the inverse t decay behavior to obtain the second asymptote. The trigonometric part in Eq. 2.6 can be estimated to be π in the region of interest of about 200nm

$$asymptote_0 = \frac{l(l+1)(n_{Layer}^2 - n_{Out}^2)^2}{4n_{Out}^2 R} t, \text{ for } \frac{t}{l_e} \ll 1 \quad (2.7)$$

$$asymptote_{+\infty} = \frac{(n_{Layer}^2 - n_{Out}^2)R}{\pi n_{Layer}^2} \frac{1}{t}, \text{ for } \frac{t}{l_e} \gg 1 \quad (2.8)$$

Equating the two and solving for t yields an approximation to the maximum enhancement point (to about 10%). In figure 2.5 the enhancement plot of a polystyrene (n = 1.6) balloon in air with two asymptotes. One can see that the two asymptotes intersect above the maximum enhancement.

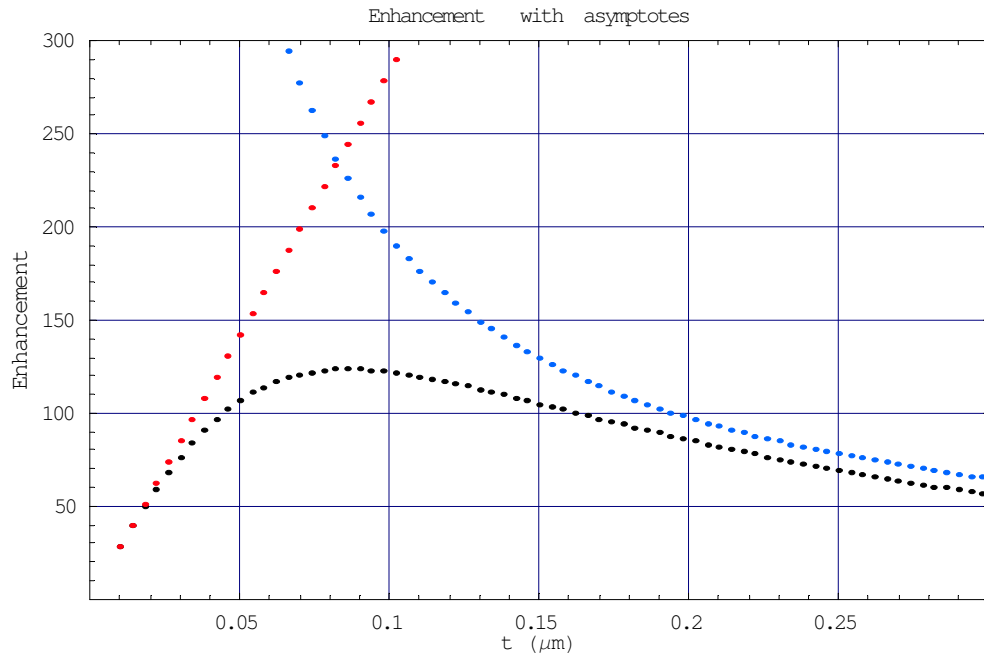


Figure 2.5 enhancement curve of polystyrene in air with the asymptotes described in Eq 2.7 and 2.8. One can see that the intersection of the two asymptotes is approximately above the maximum enhancement.

Note on the higher order modes

Previously we only considered the enhancement of a first order radial mode, however other modes will certainly appear at larger thickness. It would be no leap of faith to imagine that higher modes would have different enhancement factors. Consequently, each mode would be affected differently by adsorption which would lead to an ensemble of shifts. This can potentially be used as a molecular ruler⁵. It should not come as a surprise that the variation in the shift's magnitude for different resonances would be one of the signatures of the coated spheres (chapter 3)⁷.

In this chapter we covered the theoretical framework for enhancement of the WGM sensor. In order to simplify the analysis at an early stage of this developing research we assumed symmetry of media around the layer (the balloon). In water such symmetry may be realized in the form of a layer supported by an amorphous substrate having the refractive index of water. Several such materials are available in the form of fluorinated polymers⁸. One may even be able to pull the refractive index of the substrate below that of water. This reverse symmetry can potentially have even greater sensitivity⁹. A less exotic solution would be to support the layer with fused silica. Highly purified silica is available in optical fibers, and these can be melted to form a sphere¹⁰. A modified analysis is required to deal with this asymmetric dielectric configuration (i.e. silica, layer, water). However, the basic principle of layering for optimal sensing still holds true. In what follows we will describe our experimental approach, and present preliminary data.

Chapter 3

Experimental results

So far, the theory motivating our surface enhancement scheme has been based on a symmetric dielectric index profile ($[n_{\text{out}}, n_{\text{layer}}, n_{\text{out}}]$). In water such symmetry may be realized in the form of a layer supported by an amorphous substrate having the refractive index of water. As mentioned before, fluorinated polymers are one of several types of materials that may be employed⁸. A less exotic solution would be to support the layer with fused silica. Consequently, to preserve the layer index contrast to its surroundings a material with a refractive index higher than glass (>1.46) must be utilized. Here we found polystyrene ($n = 1.6$) to be the best candidate for preliminary experiments because of its optical characteristics and ease of use. In addition, a still higher refractive index layer ($n = 2$) was tested (Ta_2O_5) for the detection of changes in the refractive index of the surrounding aqueous medium outside.

3.1 - Making the polystyrene coated spheres

In order to fabricate polystyrene layered microspheres a simple protocol was developed. First, silica microspheres were made by melting the tip of an optical fiber to an approximate diameter of $400\mu\text{m}$ (figure 3.1a). The spheres were cleaned using Piranha solution (which hydrolyzes the surface) and then sonicated in deionized (DI) water. The sphere was subsequently dipped in di-phenyl-methyl-

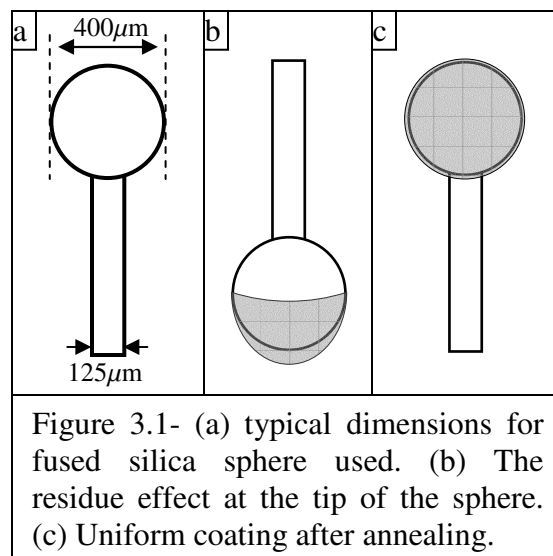
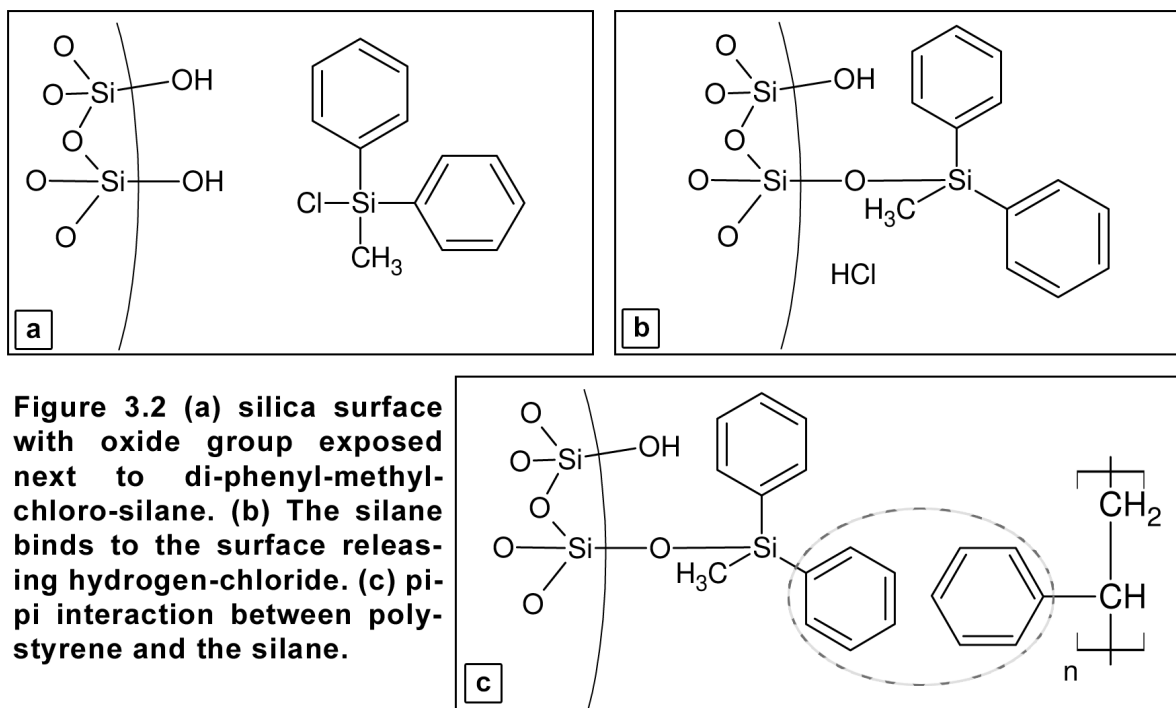


Figure 3.1- (a) typical dimensions for fused silica sphere used. (b) The residue effect at the tip of the sphere. (c) Uniform coating after annealing.

chloro-silane ($\text{CH}_3\text{Si}(\text{C}_6\text{H}_5)_2\text{Cl}$) and sonicated in methanol. This silane agent is used in order to better anchor the polystyrene coating to the silica surface (see figure 3.2). The silanol groups on the surface covalently link to silane groups by eliminating hydrogen chloride thereby extending the Si-O-Si network. After the methanol was evaporated the treated sphere was dipped into a polystyrene solution (5.3%). The solution was formed by dissolving polystyrene in xylenes. The two phenyl groups attached to the silane are said to interact with the exposed phenyls of the polystyrene (Figure 3.2c).

All of the above steps were conducted with the stem of the sphere upwards ensuring axial symmetry in the drying process. However one can imagine that the bottom half of the sphere has accumulated more styrene as the solvent was evaporating (figure 3.1b). In order to redistribute the styrene and create a uniform thin film on the surface the spheres were annealed.



In the second phase of the fabrication the spheres were oriented with their stem down and placed in an evacuation oven. This process included gradual, slow, heating while nitrogen was pumped into the oven in cycles. The reason for introducing nitrogen periodically was to minimize the presence of oxygen while annealing the styrene. After 15 minutes at 160°C the temperature was slowly brought down to room temperature. The oven pressure was raised back to 1 atmosphere (760 torr) after being sustained at about 100 torr for

the total duration of the annealing process. By annealing with the stem down, the styrene should be drawn downwards and cover the entire sphere (figure 3.1c). In addition to redistributing the layer, the annealing process is an important step to remove all excess trapped solvent (xylenes) in the styrene layer. The coated spheres were stored in a sealed container to minimize contamination.

In order to measure the coating thickness of the polystyrene film a scanning electron microscope (SEM) and an atomic force microscope (AFM) were used. Figure 3.3a shows an 8 μm AFM scan of one edge of a polystyrene film that was scratched through to allow for thickness measurement. The rectangular box in the figure represents the area that was used in figure 3.3c for step height measurement. The reason for the peak at the center of figure 3.3c can be more clearly described in figure 3.3b where a SEM image shows lips on either side of a scratch. The examined film thickness shown in figure 3.3c is $\sim 300\text{nm}$.

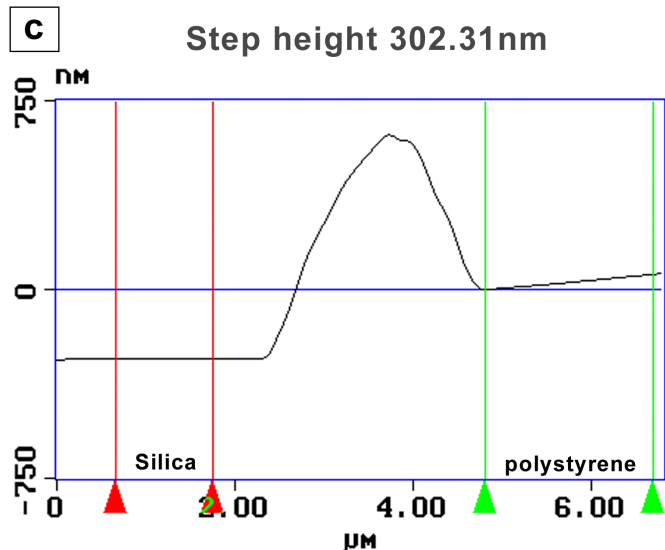
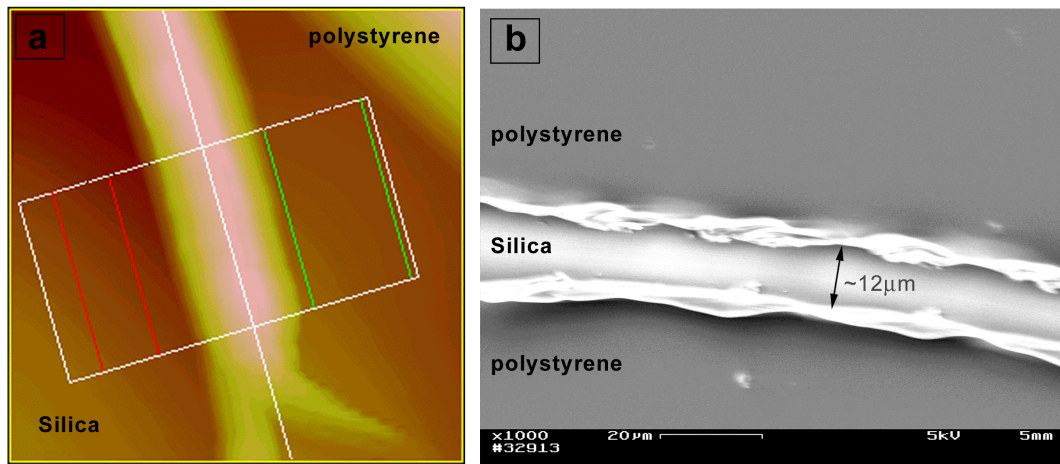


Figure 3.3 (a) an 8 μm AFM scan of one side of a 12 μm wide scratch in to a polystyrene film. (b) SEM image of a scratched polystyrene film. This shows the lips on the banks of the scratch as the polystyrene was pushed to the sides accounting for the peak in the AFM measurement (c) AFM step height measure of polystyrene after annealing.

3.2 - Experimental setup

For these experiments we employed the typical detection scheme¹¹ with slight modifications. Looking at figure 3.4a-e one can see the various components used. A pigtailed distributed feedback laser (DFB) was mounted on a rotating table to enable polarization angle selection (Figure 3.4b). The laser beam was set to propagate through a single mode optical fiber (SMF28E) which was terminated at an InGaAs detector. 15cm before the detector, the fiber's polymer coating was stripped off and the silica fiber was pulled over a butane flame. As the fiber diameter narrows down from $125\mu\text{m}$ to about $5\mu\text{m}$ more of the field is exposed to the outside, enabling coupling. The sphere was positioned in close proximity to the tapered region of the fiber. In order to mount the spheres a three dimensional manipulation stage was used (figure 3.4d). In order to conduct the experiments in aqueous media the fiber was passed through slits in opposing walls of a polystyrene cuvette. The solution does not spill through the slits due to surface tension. In order to ensure proper mixing of the solution a magnetic stir bar was placed inside the cell and stirred using another magnet turning below it (figure 3.4e).

The photo detector (figure 3.4c) which was connected through a DAQ board to a computer recorded the intensity of the laser light coming out of the fiber. If the laser was tuned to a resonance wavelength the intensity at the end of the fiber would be lower than that which is not in resonance. By scanning through wavelengths we can detect the resonance as a dip in the transmitted intensity. To do so the current source of the DFB laser was modulated using a 10Hz saw-tooth signal producing a 0.2nm scan range at around $1.3\mu\text{m}$. As analytes are introduced to the cell they interact with the evanescent field on the surface of the sphere which leads to a shift in resonance wavelength and the corresponding dips. The computer begins a data acquisition cycle by detecting a TTL pulse from the external signal generator, and detects the position of the resonant dip using a parabolic fit. The position of the dip is plotted in real-time (e.g. figure 3.6)

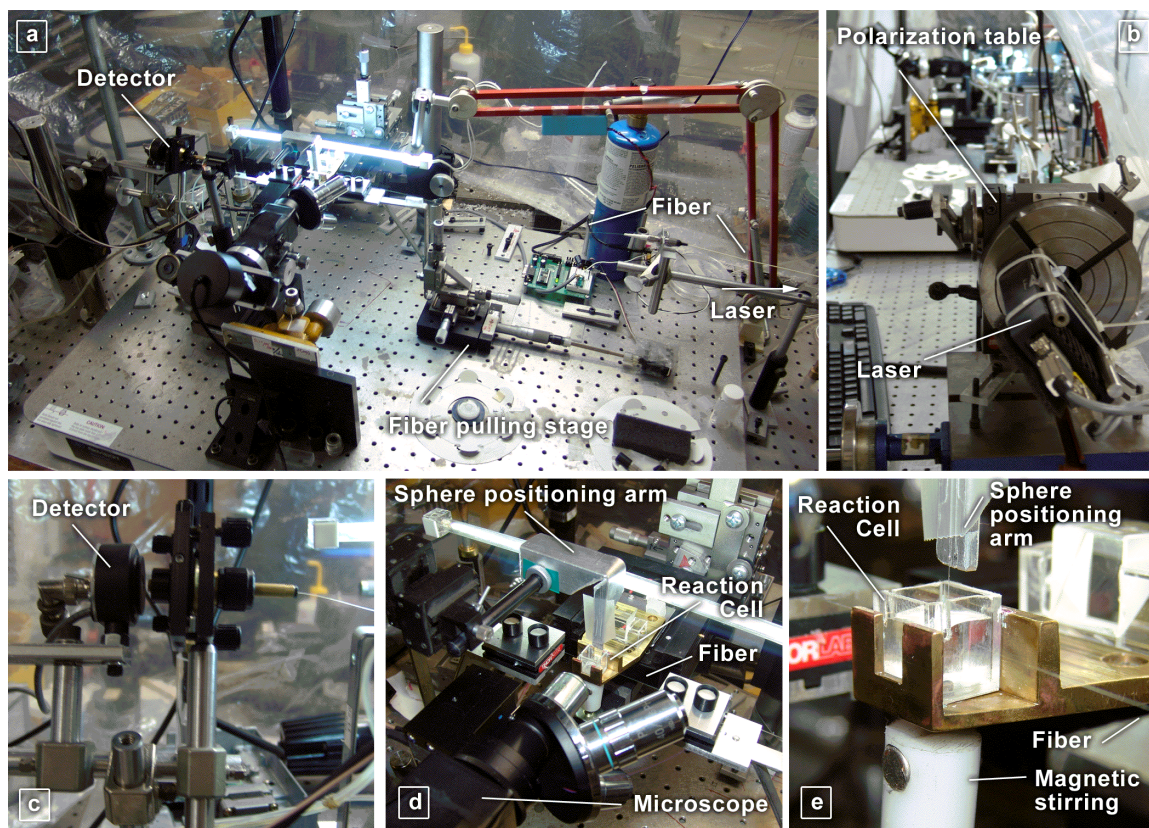


Figure 3.4 (a) experimental setup wide angle view. (b) Laser mounted on rotational stage for polarization selection. (c) The end on the fiber facing the photo detector. (d) Closer view including the reaction cell, sphere positioning arm, microscope and fiber. (e) Pulled fiber passing through a slit in the reaction cell while a sphere is mounted from the top. A magnetic bead inside the cell is rotating with the stirrer.

3.3 - Protein adsorption– BSA

Proteins serve many important functions in our bodies. For example, the interaction between proteins play a role in virus detection. As such, it is a vital step for any biosensor to be able to detect protein adsorption. Here we choose a commonly used ‘bench mark’ protein; Bovine Serum Albumin (BSA).

To understand whether our idea concerning enhancement is sound we proceeded to a fiducial experiment. The common method of treating the regular silica spheres for adsorption of BSA is by applying 3-aminopropyltrimethoxysilane (APTMS) onto the surface. At pH 7.4 this surface is positively charged while the BSA has a net negative charge enabling electrostatic attraction. The experimental results agreed with theory in the published literature¹².

In order to focus on the effects of the polystyrene layer we treated the surface differently. The isoelectric point (pI) of a protein is defined as the pH where the net charge on the protein is zero. The pI of BSA is 4.7. We can make the net charge to be positive by bringing the medium pH below 4.7. Here we conducted the experiment at pH 4.5. In order to make the surface of the polystyrene negatively charged we can simply sulfonate the exposed aromatic rings (see figure 3.5). To do so, a coated sphere was dipped in sulfuric acid for ~1 second and washed in water.

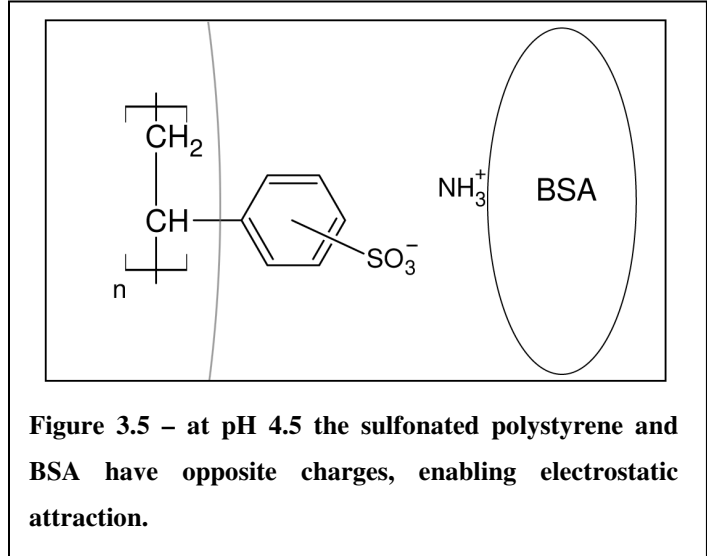


Figure 3.6 shows the normalized wavelength shift due to BSA adsorption on to a ~300nm thick polystyrene layer on a silica sphere having radius of 250 μ m. After a stable baseline was established 7 μ l of 50mM BSA was injected into 693 μ l of buffer solution with

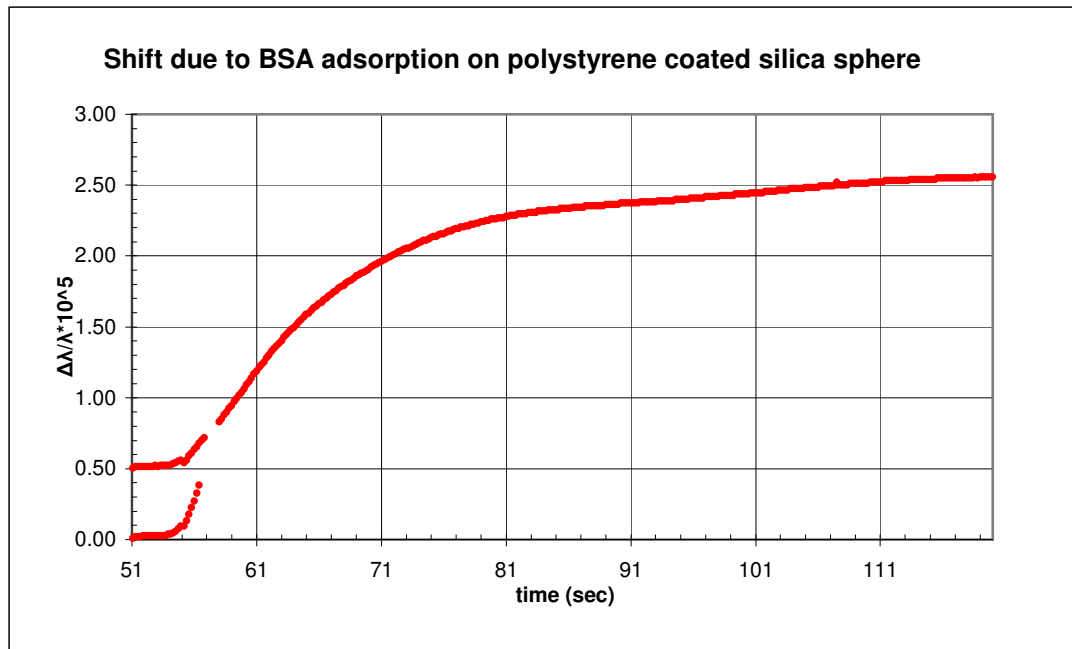


Figure 3.6 – shift due to adsorption of BSA on to polystyrene coated silica spheres¹³.

pH of 4.5 (at about the 53rd second) to make a final concentration of $\sim 500\mu\text{M}$. One can see that at first there are two parallel trace lines (at 0 and .5 vertical) this represents two separate resonances. But after the 58th second the two meet each other. This can be better understood by looking at figure 3.7. Here one can see that the two dips (resonances) are in fact merging or overlapping. This peculiar behavior is opposite to what is expected from a non-layered sphere, where all the dips shift together at about the same rate. The reason for the different behavior is that due to the redistribution of the field in the layer-sphere dielectric profile different modes are sustained with varying intensity at the surface of interaction (i.e. the adsorption site). Consequently their shifts would differ.

For an uncoated sphere of the same radius as the layered sphere ($250\mu\text{m}$), we would have expected a shift ($\delta\lambda/\lambda$) of 10^{-5} , which is 40% of what we found for the coated sphere case. We conclude that we have observed an enhancement of $\sim 250\%$ ¹³.

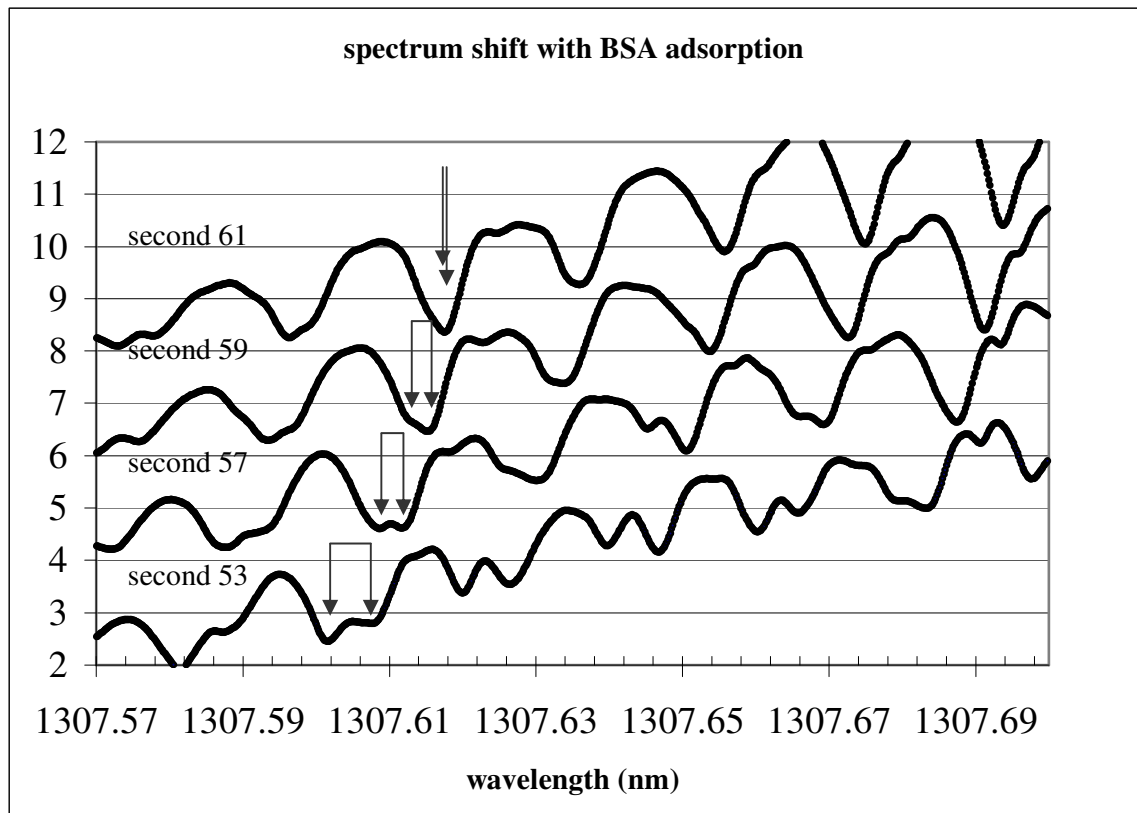


Figure 3.7 – spectrum change while BSA adsorbs to the polystyrene surface

3.4 - Index of refraction detection

Another ‘bench mark’ for a sensor is its ability to detect changes in the index of refraction of the surrounding medium. In the spirit of equation 1.3 each polarizable molecule, within the evanescent field in the surrounding medium contributes to a shift in frequency of the associated resonance. For a regular silica sphere the wavelength shift due to a slight change of refractive index Δn_m can be expressed as¹⁴

$$\frac{\Delta\lambda}{\lambda} = \frac{(\Delta n_m) n_m \lambda}{(n_s^2 - n_m^2)^{3/2} 2\pi R}, \quad (3.1)$$

To test for enhancement for this case, we compared the response of a bare sphere to that of a layered sphere. Accordingly we added to 1000 μ l DI water 3 consecutive injections of 20 μ l of 5M NaCl and recorded the shift. First we obtained the data for a bare sphere (\blacktriangle in figure 3.8). In the second set we used spheres that were coated with a 160nm thick Tantalum Pentoxide (Ta₂O₅) layer. Due to the complexity of the procedure of applying such a layer the preparation was done by a specialist coating company (Evaporated Coatings). The resulting



Figure 3.8 fractional resonance shift due to NaCl addition

shifts can be seen in figure 3.8 (■). This data clearly shows an enhancement at each concentration by a factor of two.

In this chapter we demonstrated the enhancement of resonance shift for adsorption and index of refraction change. With adsorption of bio-molecules on the surface of polystyrene on top of a silica substrate we found that the shift is about 2 and a half times the norm. In addition, for detection of changes to the media refractive index we established that the shift is double in magnitude from a homogenous sphere.

The aforementioned enhancements are clear but considerably lower than what is theoretically predicted for a 1st order mode of a dielectrically symmetric balloon (see figure 2.4). Although theory is in the works for explaining this disparity, it is likely due to two major differences in circumstances. First, the experimental microsphere is not dielectrically symmetric. Second, the polystyrene to silica refractive index contrast is lower than polystyrene to water. This implies that the field is probably shifted inward, away from the water. This effect should lead to smaller enhancement. In addition, it is likely that we have excited a mode other than a 'pure' first order mode.

Conclusion

Although a significant enhancement is seen in our measurements it is smaller than theory predicts. This disparity may be due to several factors that are not included in our model. All of these are associated with the difference between the dielectrically symmetric balloon model and the asymmetry produced by layering silica. A detailed model which goes beyond our “micro-balloon” is in the works.

Further refinement is needed in the experimental system. Presumably, optical losses due to external absorption by water at 1300nm need to be significantly reduced by moving our experiment to shorter wavelengths. A new DFB laser which operates at 780nm is being constructed as I write this.

References

- ¹ F. Vollmer, D. Braun, A Libcheaber, M Khoasima, I. Teraoka, and S. Arnold, "Protein Detection by Optical Shift of a Resonance Microcavity" *Appl. Phys. Lett.*, **80**, 4057 (2002).
- ² S. C. Hill and R. E. Benner, "Morphology-dependent resonances," in *Optical Effects Associated with Small Particles*, P. W Barber and R. K. Chang, eds. (World Scientific, Singapore, 1988).
- ³ B. R. Johnson, "Theory of morphology-dependent resonances: shape resonances and width formulas," *J. Opt. Soc. Am. A* **10**, 343-352 (1993).
- ⁴ S. Arnold, and S. Holler, "Microparticle photophysics: Fluorescence microscopy and spectroscopy of a photonic atom," in *Cavity-enhanced spectroscopies*, R D. van Zee, and J. P. Looney, eds. (Academic, San Diego, Calif., 2002), pp. 227-253
- ⁵ M. Noto, F. Vollmer, D. Keng, I. Teraoka, and S. Arnold, "Nanolayer characterization through wavelength multiplexing of a microsphere resonator," *Optics Letters* Vol. **30**, No. 5 2005 pp 510-512.
- ⁶ S. Arnold, M. Khoshsima, I. Teraoka, S. Holler, and F. Vollmer, "Shift of whispering-gallery modes in microspheres by protein adsorption" in *Optics Letters* Vol. **28** No. 4 2003 pp 272-274

-
- ⁷ I. Teraoka, S. Arnold, "Enhancing the Sensitivity of a whispering-gallery mode microsphere sensor by a high-refractive index surface layer" in J. Opt. Soc. Am. B Vol. **23** (in press 2006).
- ⁸ Y. Yang, F. Mikes, Y. Koike, and Y. Okamoto, "Synthesis and Properties of Partially Fluorinated Amorphous Ring Containing Polymers: Poly[bis(2,2-difluorovinyl)formal], poly[bis(2,2-difluorovinyl)difluoroformal], and Poly[bis(1-deuterio-2,2-difluorovinyl)difluoroformal]," *Macromolecules*, Vol. 37 7918 (2004).
- ⁹ R. Horvath, L.R. Lindvold and N.B. Larsen, "*Reverse-symmetry waveguides: theory and fabrication*", *Applied Physics B* **74**, 383 - 393 (2002).
- ¹⁰ V. B. Braginsky, M. L. Gorodetsky and V. S. Ilchenko. "Quality-factor and non-linear properties of optical whispering-gallery modes", *Physics Letters. A* **137** 393-7 (1989)
- ¹¹ G. Griffel, S. Arnold, D. Taskent, and A. Serpenguzel, "Morphology-dependent resonance of a microsphere-optical fiber system," *Optics Letters*. Vol.21 (1996).
- ¹² M. Noto, M. Khoshima, D. Keng, I. Teraoka, V. Kolchenko, and S. Arnold, "Molecular weight dependence of a whispering gallery mode biosensor," *Applied Physics Letters* **87**, (2005).
- ¹³ O. Gaathon, M. Mihnev, I. Teraoka, and S. Arnold, "Enhancement of a WGM biosensor by using nanoscopic surface layers," (in preparation, 2006).
- ¹⁴ I. Teraoka, S. Arnold, and F. Vollmer, "Perturbation approach to resonance shifts of whispering-gallery modes in a dielectric microsphere as a probe of a surrounding medium," *J. Opt. Soc. Am. B* **20**, 1937-1946 (2003).

Appendix

Appendix A
Complete derivation of the layer balloon
quantum analog (TE mode)

Part 1 (on the path to describe the field distribution in the vicinity of the layer)

Let us start from Maxwell's equations for a non-magnetic homogenous dielectric medium with no sources.

$$\nabla \cdot \mathbf{E} = 0 \quad (\text{Gauss' law for electricity}) \quad (\text{A.1})$$

$$\nabla \cdot \mathbf{B} = 0 \quad (\text{Gauss' law for magnetism}) \quad (\text{A.2})$$

$$\nabla \times \mathbf{E} = -\frac{\partial \mathbf{B}}{\partial t} \quad (\text{Faraday's law of induction}) \quad (\text{A.3})$$

$$\nabla \times \mathbf{B} = \mu_0 \varepsilon \frac{\partial \mathbf{E}}{\partial t} \quad (\text{Ampere's law}) \quad (\text{A.4})$$

We can take the curl on both sides of equation A.3 to get

$$\nabla \times \nabla \times \mathbf{E} = -\frac{\partial}{\partial t} \nabla \times \mathbf{B} \quad (\text{A.5})$$

By using equation A.4 for the $\nabla \times \mathbf{B}$ equation A.5 becomes

$$\nabla \times \nabla \times \mathbf{E} = -\frac{\partial}{\partial t} \mu_0 \varepsilon \frac{\partial \mathbf{E}}{\partial t}. \quad (\text{A.6})$$

the product of $\mu_0\epsilon$ is independent of both time and space, and $\nabla \times \nabla \times \mathbf{E}$ can be expanded, which allows us to write equation A.6 as

$$\nabla(\nabla \cdot \mathbf{E}) - \nabla^2 \mathbf{E} = -\mu_0\epsilon \frac{\partial^2 \mathbf{E}}{\partial t^2}. \quad (\text{A.7})$$

the lack of excess charge nullifies $\nabla \cdot \mathbf{E}$ (equation A.1), and reduces equation A.7 to a wave equation;

$$\nabla^2 \mathbf{E} - \mu_0\epsilon \frac{\partial^2 \mathbf{E}}{\partial t^2} = 0. \quad (\text{A.8})$$

Our system is time harmonic at all positions \mathbf{r} ,

$$\mathbf{E} = \mathbf{E}(\mathbf{r})e^{j\omega t} \quad (\text{A.9})$$

By taking the second derivative of \mathbf{E} with respect to time we can write Eq. A.8 as

$$\nabla^2 \mathbf{E}(\mathbf{r}) + \mu_0\epsilon\omega^2 \mathbf{E}(\mathbf{r}) = 0 \quad (\text{A.10})$$

we can now define two important parameters: index of refraction n and the wave number k ,

$$n = \sqrt{\frac{\epsilon}{\epsilon_0}}, \quad (\text{A.11})$$

$$k = n \frac{\omega}{c} = nk_0. \quad (\text{A.12})$$

where k_0 is the wave number in free space (i.e. $k_0 = \frac{\omega}{c}$).

Substituting this in to Eq. A.10 we get

$$\nabla^2 \mathbf{E}(\mathbf{r}) + n^2 k_0^2 \mathbf{E}(\mathbf{r}) = 0 \quad (\text{A.13})$$

the vector Helmholtz equation.

Up to now we did not force any coordinate system on the above equations. But since we are interested in a spherical structure, we choose spherical polar coordinates (i.e. r, θ, ϕ)

$$\nabla^2 = \frac{1}{r} \frac{\partial^2}{\partial r^2} r - \frac{\hat{L}^2}{r^2} \quad (\text{A.14})$$

with the angular momentum operator \hat{L} described as

$$\hat{L} = -j\mathbf{r} \times \nabla \quad (\text{A.15})$$

Together equations A.13, A.14 and A.15 gives

$$\frac{1}{r} \frac{\partial^2}{\partial r^2} r \mathbf{E}(\mathbf{r}) - \frac{\hat{L}^2}{r^2} \mathbf{E}(\mathbf{r}) + n^2 k_0^2 \mathbf{E}(\mathbf{r}) = 0. \quad (\text{A.16})$$

The angular momentum operator follows the well known commutation relationship such that

$$[\hat{L}^2, \hat{L}] = 0 \quad (\text{A.17})$$

Because of its vector form Eq. A.16 is difficult to solve. However, one of its two solutions can be constructed intuitively. Eq. A.17 suggests a trick, by setting the vector field \mathbf{E} to be the angular momentum \hat{L} operating on a scalar function ψ ,

$$\mathbf{E} = \hat{L}\psi. \quad (\text{A.18})$$

Equation A.16 can be written as

$$\hat{L} \left[\frac{1}{r} \frac{\partial^2}{\partial r^2} r \psi(\mathbf{r}) - \frac{\hat{L}^2}{r^2} \psi(\mathbf{r}) + n^2 k_0^2 \psi(\mathbf{r}) \right] = 0. \quad (\text{A.19})$$

Because the angular momentum is not zero for any of the cases we are interested in, the scalar expression being operated on in equation A.19 must be zero,

$$\frac{\partial^2}{\partial r^2} [r\psi(\mathbf{r})] - \frac{\hat{L}^2}{r^2} [r\psi(\mathbf{r})] + n^2 k_0^2 [r\psi(\mathbf{r})] = 0. \quad (\text{A.20})$$

Since the refractive index will be spherically symmetric in our case, and is linear, the wave function $\psi(\mathbf{r})$ can be separated into radial and angular parts,

$$\psi(\mathbf{r}) = \psi(r)Y_{lm}(\theta, \phi) \quad (\text{A.21})$$

Where $Y_{lm}(\theta, \phi)$ are spherical harmonics associated with a polar angle (θ) and the azimuthal angle (ϕ).

Equation A.21 is simplified by defining a new scalar function,

$$\psi_r(r) = r\psi(r). \quad (\text{A.22})$$

such that

$$\frac{\partial^2}{\partial r^2} \psi_r(r)Y(\theta, \phi)_{l,m} - \frac{l(l+1)}{r^2} \psi_r(r)Y(\theta, \phi)_{l,m} + n^2 k_0^2 \psi_r(r)Y(\theta, \phi)_{l,m} = 0 \quad (\text{A.23})$$

Again, we can pull out the angular part as we would never see it go to zero

$$\frac{\partial^2}{\partial r^2} \psi_r(r) - \frac{l(l+1)}{r^2} \psi_r(r) + n^2 k_0^2 \psi_r(r) = 0 \quad (\text{A.24})$$

which is now in a complete scalar form. Rewriting this in to a more familiar form

$$\frac{\partial^2}{\partial r^2} \psi_r(r) + \left[n^2 k_0^2 - \frac{l(l+1)}{r^2} \right] \psi_r(r) = 0 \quad (\text{A.25})$$

Here we can do a neat trick. Let's add and subtract k_0^2 from the second term and write it in the following way,

$$\frac{\partial^2}{\partial r^2} \psi_r(r) + \left[k_0^2 - \left((1-n^2)k_0^2 + \frac{l(l+1)}{r^2} \right) \right] \psi_r(r) = 0. \quad (\text{A.26})$$

Doesn't this resemble the time independent Schrödinger equation (with $\frac{2m}{\hbar^2} = 1$)?

$$\frac{\partial^2}{\partial r^2} \psi_r(r) + \left[\mathcal{E}_{eff} - V_{eff} \right] \psi_r(r) = 0 \quad (\text{A.27})$$

with the effective energy $\mathcal{E}_{eff} = k_0^2$ and the effective potential

$$V_{eff} = k_0^2 (1 - n^2) + \frac{l(l+1)}{r^2}. \quad (\text{A.28})$$

It is no leap of imagination to think of a one dimensional finite well with the same governing equation. Taking the case of a single particle bouncing between the two walls we can describe the probability function in terms of position ψ_r (figure A.1).

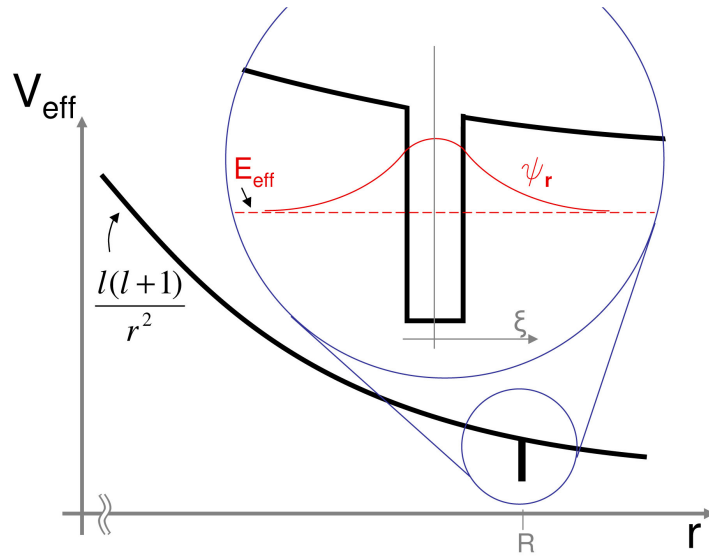


Figure A.1: the radial part of the potential in a balloon. The change in the index of refraction creates the notch around position R . The potential falls like the square of $1/r$. In the insert- illustration of the distribution of the probability function ψ and its exponential decay outside of the layer.

For simplicity we can shift the coordinates to the center of the well.

$$\xi = r - R \quad (\text{A.29})$$

In addition, we should verify that the derivative is sound.

$$\frac{d\psi}{dr} = \frac{d\psi}{d\xi} \frac{d\xi}{dr} = \frac{d\psi}{d\xi} \quad (\text{A.30})$$

$$\frac{d}{dr} \left(\frac{d\psi}{d\xi} \right) = \frac{d}{d\xi} \left(\frac{d\psi}{d\xi} \right) \frac{d\xi}{dr} = \frac{d^2\psi}{d\xi^2} \quad (\text{A.31})$$

And now we have the function in terms of ξ

$$\frac{d^2\psi}{d\xi^2} + [\mathcal{E}_{\text{eff}}^{\circ} - V_{\text{eff}}(\xi)]\psi = 0 \quad (\text{A.32})$$

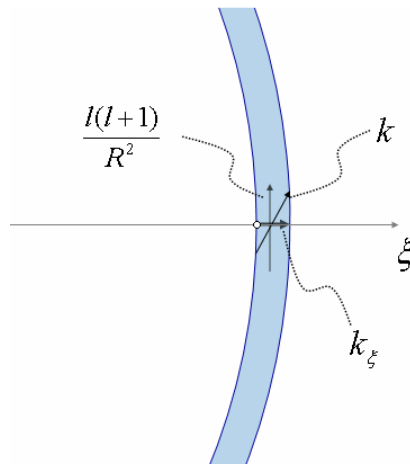


Figure A.2 the different components of vector \mathbf{k} inside the layer (top view).

Above is a close up of the layer where \mathbf{k} is the propagation vector inside the film. We can take \mathbf{k} apart in to its orthogonal components (in spherical coordinates) where

$$k^2 = k_\xi^2 + k_\phi^2 \quad (\text{A.33})$$

or

$$k_0^2 n^2 = k_\xi^2 + k_\phi^2 \quad (\text{A.34})$$

The ϕ component of \mathbf{k} is simply the centripetal part at the center of the layer

$$k_\phi^2 = \frac{l(l+1)}{R^2} \quad (\text{A.35})$$

also for resonance we have to complete an integer number of wavelengths so:

$$k_\phi = \frac{2\pi}{\lambda_c} \quad (\text{A.36})$$

When looking at the function inside the layer we can identify a solution to the differential equation coming from

$$k_\xi^2 = k_0^2 n_{Layer}^2 - \frac{l(l+1)}{R^2} \quad (\text{A.37})$$

in the form of

$$\psi_{Layer} \approx e^{\pm j k_\xi \xi} \quad (\text{A.38})$$

When looking at the function outside the layer (although in the symmetric case either side is fine we will focus on $\xi > \frac{t}{2}$)

$$\epsilon_{eff} - V_{eff} = k_0^2 n_{Out}^2 - \frac{l(l+1)}{R^2} \quad (\text{A.39})$$

Outside the potential is greater then the energy. One can anticipate a negative value under the root. To simplify, we would just flip the terms and take j out.

$$\kappa^2 = -k_0^2 n_{Out}^2 + \frac{l(l+1)}{R^2} \quad (\text{A.40})$$

$$\psi_{Out} \approx e^{\pm j j \kappa \xi} \Rightarrow e^{-\kappa \xi} \quad (\text{A.41})$$

(We do not take the + sign to be a feasible option as it is not physical: the field can not become greater as you move away from the source).

To comply with the boundary condition the solution inside and outside must agree.

$$\psi_{Layer} = \psi_{Out} \quad (A.42)$$

Also, the derivative on both sides of the boundary must be the same to allow for continuity.

$$\frac{d\psi_{Layer}}{d\xi} = \frac{d\psi_{Out}}{d\xi} \quad (A.43)$$

That is at $\pm t/2$ the logarithmic derivative ought to be equal.

$$\frac{1}{\psi_{Layer}} \frac{d\psi_{Layer}}{d\xi} = \frac{1}{\psi_{Out}} \frac{d\psi_{Out}}{d\xi} \quad (A.44)$$

evaluating ψ at both sides of the boundary yields

$$\psi_{Layer} \approx Ae^{\pm jk_\xi \xi} \approx A \cos(k_\xi \xi) \quad (A.45)$$

$$\frac{1}{\psi_{Layer}} \frac{d\psi_{Layer}}{d\xi} \Big|_{t/2} \approx \frac{-Ak_\xi \sin(k_\xi \xi)}{A \cos(k_\xi \xi)} \Big|_{t/2} = -k_\xi \tan(k_\xi \xi) \Big|_{t/2} \quad (A.46)$$

$$\frac{1}{\psi_{Layer}} \frac{d\psi_{Layer}}{d\xi} \Big|_{t/2} \approx -k_\xi \tan\left(k_\xi \frac{t}{2}\right) \quad (A.47)$$

for the inside. And for the outside part

$$\psi_{Out} \approx Be^{-\kappa \xi} \quad (A.48)$$

$$\frac{1}{\psi_{Out}} \frac{d\psi_{Out}}{d\xi} \approx \frac{-\kappa Be^{-\kappa \xi}}{Be^{-\kappa \xi}} = -\kappa \quad (A.49)$$

So, at the surface

$$-k_{\xi} \tan\left(k_{\xi} \frac{t}{2}\right) = -\kappa \quad (\text{A.50})$$

Or

$$\tan\left(k_{\xi} \frac{t}{2}\right) = \frac{\kappa}{k_{\xi}} \quad (\text{A.51})$$

in order to have similar terms on the left and right side of equation A.51 we can add $t/2$ to both the numerator and denominator on the right. If one Square equation A.51 the exponential decay factor κ can be easily replaced by using equation A.40 to

$$\tan^2\left(k_{\xi} \frac{t}{2}\right) = \frac{\kappa^2 \left(\frac{t}{2}\right)^2}{k_{\xi}^2 \left(\frac{t}{2}\right)^2} = \frac{[k_{\phi}^2 - n_{Out}^2 k_0^2] \left(\frac{t}{2}\right)^2}{k_{\xi}^2 \left(\frac{t}{2}\right)^2}. \quad (\text{A.52})$$

One can go further and replace the square of k_0 with the components in equation A.37

$$\tan^2\left(k_{\xi} \frac{t}{2}\right) = \frac{\left[k_{\phi}^2 - n_{Out}^2 \frac{(k_{\xi}^2 + k_{\phi}^2)}{n_{Layer}^2} \right] \left(\frac{t}{2}\right)^2}{k_{\xi}^2 \left(\frac{t}{2}\right)^2}. \quad (\text{A.53})$$

Rearranging the numerator we get

$$\frac{\left[k_{\phi}^2 \left(1 - \frac{n_{Out}^2}{n_{Layer}^2} \right) - \frac{n_{Out}^2}{n_{Layer}^2} k_{\xi}^2 \right] \left(\frac{t}{2}\right)^2}{k_{\xi}^2 \left(\frac{t}{2}\right)^2} = \frac{n_{Out}^2}{n_{Layer}^2} \left[\frac{k_{\phi}^2 \left(\frac{n_{Layer}^2}{n_{Out}^2} - 1 \right) \left(\frac{t}{2}\right)^2}{k_{\xi}^2 \left(\frac{t}{2}\right)^2} - 1 \right]. \quad (\text{A.54})$$

defining

$$n_{Relative} = \frac{n_{Layer}}{n_{Out}} \quad (A.55)$$

we can rewrite equation A.53 as

$$\tan(z) = \frac{1}{n_{Relative}} \sqrt{\frac{z_{max}^2}{z^2} - 1}, \quad (A.56)$$

where

$$z = k_{\xi} \frac{t}{2}, \quad (A.57)$$

and

$$z_{max}^2 = k_{\phi}^2 \left(\frac{t}{2}\right)^2 (n_{Relative}^2 - 1). \quad (A.58)$$

As a side note, like any transcendental equation the solutions cannot come in analytic form and requires a numerical solution. But a linear approximation (i.e. $\tan(z) = z$) can be made in equation A.56 enabling z to be evaluated as

$$z^2 \approx \frac{\left[1 + 4n_{Relative}^2 z_{max}^2\right]^{\frac{1}{2}} - 1}{2n_{Relative}^2}. \quad (A.59)$$

Rewriting equations A.34 in terms of z produces

$$k_0^2 = \frac{z^2 \left(\frac{2}{t}\right)^2 + \frac{l(l+1)}{R^2}}{n_{Relative}^2}. \quad (A.60)$$

Plugging equation A.60 into equation A.40 we get

$$\kappa^2 = \frac{-z^2 \left(\frac{2}{t}\right)^2 - \frac{l(l+1)}{R^2}}{n_{Relative}^2} + \frac{l(l+1)}{R^2} \quad (\text{A.61})$$

which can be simplified to be

$$n_{Relative}^2 \kappa^2 = -z^2 \left(\frac{2}{t}\right)^2 + (n_{Relative}^2 - 1) \frac{l(l+1)}{R^2} = -z^2 \left(\frac{2}{t}\right)^2 + z_{\max}^2 \left(\frac{2}{t}\right)^2. \quad (\text{A.62})$$

By multiplying equation A.62 by $(t/2)^2$ it is made dimensionless

$$n_{Relative}^2 \kappa^2 \left(\frac{t}{2}\right)^2 = z_{\max}^2 - z^2. \quad (\text{A.63})$$

As κ is the reciprocal of the characteristic length of the evanescent field l_e we get

$$l_e^2 = \frac{n_{Relative}^2 \left(\frac{t}{2}\right)^2}{z_{\max}^2 - z^2}. \quad (\text{A.64})$$

As in any finite well problem the characteristic length of the evanescent field l_e is a measure of the probability of finding a photon outside the well. Although equation A.64 cannot be solved without going back to the transcendental relations above, it still may provide us with some insight in to the distribution of the wave function and its competing parameters. By varying the well width (i.e. layer thickness) and its depth (i.e. index contrast) we can control the penetration length of the evanescent field outside. As the well width narrows z increases (i.e. climbs up the well) which promotes larger characteristic length. At the limit when the well is infinitesimally small z approach z_{\max} and the characteristic length expands to infinity.

PART 2

(looking for enhancement)

The method by which we sense adsorption or proximity of analytes to our system is by monitoring the resonance spectrum of the cavity (sphere, disk, ring or balloon). The general theoretical model for adsorption is built up from adsorption of a single particle at position \mathbf{r}_i . In its essence, the resonance shift in frequency is the interaction of the particle with the evanescent field at the surface relative to the total energy of the mode,

$$\frac{\delta\omega}{\omega} = \frac{-\alpha |E_0(\mathbf{r}_i)|^2}{2 \int \epsilon(\mathbf{r}_i) |E_0(\mathbf{r}_i)|^2 dV} \quad (\text{A.65})$$

where α is the polarizability of the molecule. In the spherical geometry at hand $E_0(\mathbf{r}_i)$ can be written out in terms of its radial and angular parts such that;

$$\frac{\delta\omega}{\omega} = \frac{-\alpha (f(r))^2 |\hat{L}Y_{ll}|^2}{2 \int \epsilon_0 (n(r))^2 (f(r))^2 |\hat{L}Y_{ll}|^2 dV} \quad (\text{A.66})$$

$$\approx \frac{-\alpha (f(r))^2 |Y_{ll}|^2}{2 \int \epsilon_0 (n(r))^2 (f(r))^2 r^2 dr \int |Y_{ll}|^2 d\Omega} \quad (\text{A.67})$$

for Y_{ll}^2 function is normalized (i.e. $\int |Y_{ll}|^2 d\Omega = 1$), and Eq. A.67 is simplified to

$$\frac{\delta\omega}{\omega} = \frac{-\alpha (f(r))^2 |Y_{ll}|^2}{2 \int \epsilon_0 (n(r))^2 (f(r))^2 r^2 dr}. \quad (\text{A.68})$$

Let us shift the coordinates back to ξ

$$r = R + \xi \quad (\text{A.69})$$

$$dr = d\xi \quad (\text{A.70})$$

under the conditions examined $\xi \ll R$, and $r^2 \approx R^2$ and

$$\frac{\delta\omega}{\omega} \approx \frac{-\alpha (f(\xi))^2 |Y_{ll}|^2}{2R^2 \epsilon_0 \int (n(\xi))^2 (f(\xi))^2 d\xi} \quad (\text{A.71})$$

The denominator D can be split in to two parts associated with the interior and exterior of the balloon's skin. With the interior having refractive index n_{Layer} and exterior n_{Out} , the denominator becomes

$$D = 2\epsilon_0 R^2 \left[\int n_{\text{Layer}}^2 (f(\xi))^2 d\xi + \int n_{\text{Out}}^2 (f(\xi))^2 d\xi \right] \quad (\text{A.72})$$

Within the layer the first integral in Eq.A.72, using equation A.45 is

$$\int n_{\text{Layer}}^2 (f(\xi))^2 d\xi = n_{\text{Layer}}^2 A^2 \int_{-\frac{t}{2}}^{\frac{t}{2}} \cos^2(k_\xi \xi) d\xi = n_{\text{Layer}}^2 A^2 \left[\frac{t}{2} + \frac{\sin(k_\xi t)}{2k_\xi} \right]. \quad (\text{A.73})$$

The second integral in A.72 using equation A.48 is

$$\int n_{\text{Out}}^2 (f(\xi))^2 d\xi = n_{\text{Out}}^2 2B^2 \int_{\frac{t}{2}}^{\infty} e^{-2\kappa\xi} d\xi = \frac{n_{\text{Out}}^2}{\kappa} B^2 e^{-\kappa t} = l_e n_{\text{Out}}^2 \left(f\left(\frac{t}{2}\right) \right)^2. \quad (\text{A.74})$$

The resonant shift in A.71 after using A.73 and A.74 is

$$\frac{\delta\omega}{\omega} = \frac{-\alpha \left(f\left(\frac{t}{2}\right) \right)^2 |Y_{ll}|^2}{2\epsilon_0 R^2 \left[n_{\text{Layer}}^2 A^2 \left[\frac{t}{2} + \frac{\sin(k_\xi t)}{2k_\xi} \right] + l_e n_{\text{Out}}^2 \left(f\left(\frac{t}{2}\right) \right)^2 \right]}. \quad (\text{A.75})$$

Dividing top and bottom by $\left(f\left(\frac{t}{2}\right) \right)^2$ we get

$$\frac{\delta\omega}{\omega} = \frac{-\alpha |Y_{ll}|^2}{2\epsilon_0 R^2 \left[n_{\text{Layer}}^2 \frac{A^2}{\left(f\left(\frac{t}{2}\right) \right)^2} \left[\frac{t}{2} + \frac{2 \sin(k_\xi \frac{t}{2}) \cos(k_\xi \frac{t}{2})}{2k_\xi} \right] + l_e n_{\text{Out}}^2 \right]}. \quad (\text{A.76})$$

Now, let us evaluate $\frac{A^2}{(f(\frac{t}{2}))^2}$ at the boundary,

$$\frac{A^2}{(f(\frac{t}{2}))^2} = \frac{A^2}{A^2 \cos^2(k_\xi \xi)} \Big|_{\xi=\frac{t}{2}} = \frac{1}{\cos^2(k_\xi \frac{t}{2})}. \quad (\text{A.77})$$

equation A.76 now becomes

$$\frac{\delta\omega}{\omega} = \frac{-\alpha |Y_{ll}|^2}{\epsilon_0 R^2 \left[n_{Layer}^2 t \left[\sec^2(k_\xi \frac{t}{2}) + \frac{\tan(k_\xi \frac{t}{2})}{k_\xi \frac{t}{2}} \right] + 2l_e n_{Out}^2 \right]}. \quad (\text{A.78})$$

Remember that

$$z = k_\xi \frac{t}{2} \quad (\text{A.79})$$

we can rewrite A.79 in terms of z

$$\frac{\delta\omega}{\omega} = \frac{-\alpha |Y_{ll}|^2}{\epsilon_0 R^2 \left[n_{Layer}^2 t \left[\sec^2(z) + \frac{\tan(z)}{z} \right] + 2l_e n_{Out}^2 \right]}. \quad (\text{A.80})$$

In chapter 1 we recalled that $\frac{\delta\omega}{\omega}$ for the solid sphere case (Eq.1.4),

$$\frac{\delta\omega}{\omega} \approx \frac{-\alpha |Y_{ll}|^2}{\epsilon_0 R^3 (n_{Layer}^2 - n_{Out}^2)}. \quad (\text{A.81})$$

Now we can define the enhancement as the relative shift in the layer structure to the one if a sphere were had been made from the same dielectric

$$\mathcal{E} = \frac{\left(\frac{\delta\omega}{\omega} \right)_{Layer}}{\left(\frac{\delta\omega}{\omega} \right)_{Solid}} \quad (\text{A.82})$$

Substituting in the various elements we get

$$\mathcal{E} = \frac{\epsilon_0 R^3 (n_{Layer}^2 - n_{Out}^2)}{\epsilon_0 R^2 \left[n_{Layer}^2 t \left[\sec^2(z) + \frac{\tan(z)}{z} \right] + 2l_e n_{Out}^2 \right]}. \quad (\text{A.83})$$

Which finally can be written as

$$\mathcal{E} = \frac{(n_{Layer}^2 - n_{Out}^2) R}{n_{Layer}^2 t \left[\sec^2(z) + \frac{\tan(z)}{z} \right] + 2n_{Out}^2 l_e}. \quad (\text{A.84})$$

Appendix B

Experimental protocols and technical information

Total weight of 2.0068g gives us 5.3% Polystyrene in 40ml xylenes

- Hold spheres upside down
- 7 min piranha solution
 - 3 x Hydrogen Peroxide
 - 7 x Sulfuric Acid (concentrated)
- ~1 min sonicated in ID water
- Dip in Di-Phenyl-Methyl-Chloro-Silane (1 min)
- ~1 min sonicated in Methanol
- Dip in 5.3% Polystyrene in xylenes
- Let hang for a few seconds (to dry out the xylenes)
- Flip over (so that the stem is below)

Successful baking recipe:

Time	Duration	Setting	Temp	Comments
0	15 min	1		a) While door is slightly open pump Nitrogen in. b) Close door and turn vacuum on. Bring pressure down to 15" Hg c) Shutdown Nitrogen and after pressure is down- stop vacuum.
15	15 min	1.75	40°C	
30	15 min	2.5	65°C	a) turn vacuum on b) pump Nitrogen in c) Shutdown Nitrogen and after pressure is down- stop vacuum
45	85 min	3	85°C	
130	35 min	2	155°C	a) turn vacuum on. b) pump Nitrogen in c) Shutdown Nitrogen and after pressure is down- stop vacuum
165	15 min	2.6	145°C	
180	30 min	0	155°C	a) pump Nitrogen in b) open door to bring temperature down
210	10	0	125°C	
220			105°C	
			Room	Try to bring chamber down to room temperature before taking out

Place in a glass vessel that Nitrogen was blown into it before.

Appendix C

Mathematica Script

In[1]:=

```
<< Graphics`Graphics`;  
<< Graphics`MultipleListPlot`;  
Off[General::spell]  
  
Parameters;  
nLayer = 1.6; nOut = 1; nR = nLayer/nOut;  
R = 100 * 10^-6;  
l = 683;  
  
tSTART = 25 * 10^-9; tEND = 500 * 10^-9; tINC = 5 * 10^-9;  
  
tTABLE = N[Table[t, {t, tSTART, tEND, tINC}]]  
tTABLE $\mu$  = tTABLE * 10^6;
```

Out[9]=

```
{2.5 × 10-8, 3. × 10-8, 3.5 × 10-8, 4. × 10-8, 4.5 × 10-8, 5. × 10-8, 5.5 × 10-8, 6. × 10-8,  
6.5 × 10-8, 7. × 10-8, 7.5 × 10-8, 8. × 10-8, 8.5 × 10-8, 9. × 10-8, 9.5 × 10-8, 1. × 10-7,  
1.05 × 10-7, 1.1 × 10-7, 1.15 × 10-7, 1.2 × 10-7, 1.25 × 10-7, 1.3 × 10-7, 1.35 × 10-7, 1.4 × 10-7,  
1.45 × 10-7, 1.5 × 10-7, 1.55 × 10-7, 1.6 × 10-7, 1.65 × 10-7, 1.7 × 10-7, 1.75 × 10-7, 1.8 × 10-7,  
1.85 × 10-7, 1.9 × 10-7, 1.95 × 10-7, 2. × 10-7, 2.05 × 10-7, 2.1 × 10-7, 2.15 × 10-7, 2.2 × 10-7,  
2.25 × 10-7, 2.3 × 10-7, 2.35 × 10-7, 2.4 × 10-7, 2.45 × 10-7, 2.5 × 10-7, 2.55 × 10-7, 2.6 × 10-7,  
2.65 × 10-7, 2.7 × 10-7, 2.75 × 10-7, 2.8 × 10-7, 2.85 × 10-7, 2.9 × 10-7, 2.95 × 10-7, 3. × 10-7,  
3.05 × 10-7, 3.1 × 10-7, 3.15 × 10-7, 3.2 × 10-7, 3.25 × 10-7, 3.3 × 10-7, 3.35 × 10-7, 3.4 × 10-7,  
3.45 × 10-7, 3.5 × 10-7, 3.55 × 10-7, 3.6 × 10-7, 3.65 × 10-7, 3.7 × 10-7, 3.75 × 10-7, 3.8 × 10-7,  
3.85 × 10-7, 3.9 × 10-7, 3.95 × 10-7, 4. × 10-7, 4.05 × 10-7, 4.1 × 10-7, 4.15 × 10-7, 4.2 × 10-7,  
4.25 × 10-7, 4.3 × 10-7, 4.35 × 10-7, 4.4 × 10-7, 4.45 × 10-7, 4.5 × 10-7, 4.55 × 10-7, 4.6 × 10-7,  
4.65 × 10-7, 4.7 × 10-7, 4.75 × 10-7, 4.8 × 10-7, 4.85 × 10-7, 4.9 × 10-7, 4.95 × 10-7, 5. × 10-7}
```

In[11]:=

```

s2 =  $\frac{1(1+1)}{(R)^2} \left( 1 - \left( \frac{nOut}{nLayer} \right)^2 \right) \left( \frac{t}{2} \right)^2;$ 
kft2TABLE =
Table[FindRoot[Tan[s1] == Sqrt[s2/s1^2 -  $\left( \frac{nOut}{nLayer} \right)^2$ ],
{s1, 10^-11}], {t, tSTART, tEND, tINC}];
kft2LIST = s1 /. kft2TABLE ;
kflIST = 2 + kft2LIST / tTABLE
k0 = Re[Sqrt[(kflIST^2 + 1(1+1) / (R)^2) / nLayer^2]];
k0TABLE = Transpose[{tTABLE, k0}];
κ = Sqrt[-k0^2 + nOut^2 + 1(1+1) / (R)^2]
γ = kft2LIST ;
Γ = 1 / κ

```

Out[14]=

```

{8.41758 × 106, 8.36807 × 106, 8.31166 × 106, 8.24922 × 106, 8.18157 × 106, 8.10954 × 106,
8.03391 × 106, 7.95539 × 106, 7.87464 × 106, 7.79222 × 106, 7.70866 × 106, 7.6244 × 106,
7.53983 × 106, 7.45527 × 106, 7.371 × 106, 7.28726 × 106, 7.20422 × 106, 7.12206 × 106,
7.04089 × 106, 6.96082 × 106, 6.88193 × 106, 6.80428 × 106, 6.72791 × 106, 6.65285 × 106,
6.57913 × 106, 6.50676 × 106, 6.43574 × 106, 6.36606 × 106, 6.29772 × 106, 6.2307 × 106,
6.165 × 106, 6.10058 × 106, 6.03743 × 106, 5.97552 × 106, 5.91484 × 106, 5.85535 × 106,
5.79704 × 106, 5.73986 × 106, 5.68381 × 106, 5.62884 × 106, 5.57494 × 106, 5.52208 × 106,
5.47023 × 106, 5.41937 × 106, 5.36947 × 106, 5.3205 × 106, 5.27245 × 106, 5.22529 × 106,
5.17899 × 106, 5.13354 × 106, 5.08892 × 106, 5.04509 × 106, 5.00204 × 106, 4.95976 × 106,
4.91821 × 106, 4.87739 × 106, 4.83727 × 106, 4.79784 × 106, 4.75907 × 106, 4.72096 × 106,
4.68348 × 106, 4.64662 × 106, 4.61037 × 106, 4.57471 × 106, 4.53962 × 106, 4.50509 × 106,
4.47111 × 106, 4.43766 × 106, 4.40474 × 106, 4.37233 × 106, 4.34041 × 106, 4.30898 × 106,
4.27802 × 106, 4.24753 × 106, 4.21749 × 106, 4.18789 × 106, 4.15873 × 106, 4.12999 × 106,
4.10166 × 106, 4.07374 × 106, 4.04621 × 106, 4.01907 × 106, 3.99231 × 106, 3.96593 × 106,
3.9399 × 106, 3.91423 × 106, 3.88891 × 106, 3.86392 × 106, 3.83927 × 106, 3.81495 × 106,
3.79095 × 106, 3.76726 × 106, 3.74388 × 106, 3.7208 × 106, 3.69801 × 106, 3.67552 × 106}

```

Out[17]=

```
{888979., 1.05592 × 106, 1.21756 × 106, 1.37348 × 106, 1.52335 × 106, 1.66702 × 106,
1.80441 × 106, 1.93554 × 106, 2.06051 × 106, 2.17946 × 106, 2.2926 × 106, 2.40014 × 106,
2.50233 × 106, 2.59941 × 106, 2.69165 × 106, 2.7793 × 106, 2.86261 × 106, 2.94183 × 106,
3.01718 × 106, 3.0889 × 106, 3.1572 × 106, 3.22228 × 106, 3.28432 × 106, 3.34351 × 106,
3.40001 × 106, 3.45399 × 106, 3.50558 × 106, 3.55493 × 106, 3.60217 × 106, 3.64741 × 106,
3.69076 × 106, 3.73234 × 106, 3.77224 × 106, 3.81055 × 106, 3.84736 × 106, 3.88274 × 106,
3.91677 × 106, 3.94952 × 106, 3.98107 × 106, 4.01146 × 106, 4.04075 × 106, 4.06901 × 106,
4.09627 × 106, 4.1226 × 106, 4.14803 × 106, 4.1726 × 106, 4.19636 × 106, 4.21934 × 106,
4.24157 × 106, 4.2631 × 106, 4.28395 × 106, 4.30415 × 106, 4.32373 × 106, 4.34272 × 106,
4.36114 × 106, 4.37901 × 106, 4.39636 × 106, 4.41321 × 106, 4.42957 × 106, 4.44548 × 106,
4.46093 × 106, 4.47597 × 106, 4.49059 × 106, 4.50481 × 106, 4.51866 × 106, 4.53213 × 106,
4.54526 × 106, 4.55804 × 106, 4.5705 × 106, 4.58264 × 106, 4.59448 × 106, 4.60602 × 106,
4.61728 × 106, 4.62826 × 106, 4.63898 × 106, 4.64945 × 106, 4.65966 × 106, 4.66963 × 106,
4.67938 × 106, 4.68889 × 106, 4.6982 × 106, 4.70729 × 106, 4.71617 × 106, 4.72486 × 106,
4.73336 × 106, 4.74167 × 106, 4.7498 × 106, 4.75776 × 106, 4.76555 × 106, 4.77317 × 106,
4.78064 × 106, 4.78795 × 106, 4.79511 × 106, 4.80212 × 106, 4.80899 × 106, 4.81572 × 106}
```

Out[19]=

```
{1.12489 × 10-6, 9.47042 × 10-7, 8.21312 × 10-7, 7.2808 × 10-7, 6.56447 × 10-7, 5.99873 × 10-7,
5.54198 × 10-7, 5.16652 × 10-7, 4.85318 × 10-7, 4.58829 × 10-7, 4.36186 × 10-7, 4.16643 × 10-7,
3.99628 × 10-7, 3.84703 × 10-7, 3.71519 × 10-7, 3.59803 × 10-7, 3.49331 × 10-7, 3.39925 × 10-7,
3.31435 × 10-7, 3.23739 × 10-7, 3.16736 × 10-7, 3.1034 × 10-7, 3.04477 × 10-7, 2.99087 × 10-7,
2.94116 × 10-7, 2.8952 × 10-7, 2.85259 × 10-7, 2.81299 × 10-7, 2.77611 × 10-7, 2.74167 × 10-7,
2.70947 × 10-7, 2.67928 × 10-7, 2.65094 × 10-7, 2.62429 × 10-7, 2.59919 × 10-7, 2.5755 × 10-7,
2.55312 × 10-7, 2.53195 × 10-7, 2.51189 × 10-7, 2.49286 × 10-7, 2.47479 × 10-7, 2.4576 × 10-7,
2.44124 × 10-7, 2.42565 × 10-7, 2.41079 × 10-7, 2.39659 × 10-7, 2.38302 × 10-7, 2.37004 × 10-7,
2.35762 × 10-7, 2.34571 × 10-7, 2.33429 × 10-7, 2.32334 × 10-7, 2.31282 × 10-7, 2.3027 × 10-7,
2.29298 × 10-7, 2.28362 × 10-7, 2.27461 × 10-7, 2.26593 × 10-7, 2.25755 × 10-7, 2.24948 × 10-7,
2.24168 × 10-7, 2.23416 × 10-7, 2.22688 × 10-7, 2.21985 × 10-7, 2.21305 × 10-7, 2.20647 × 10-7,
2.20009 × 10-7, 2.19392 × 10-7, 2.18794 × 10-7, 2.18215 × 10-7, 2.17652 × 10-7, 2.17107 × 10-7,
2.16578 × 10-7, 2.16064 × 10-7, 2.15564 × 10-7, 2.15079 × 10-7, 2.14608 × 10-7, 2.1415 × 10-7,
2.13704 × 10-7, 2.1327 × 10-7, 2.12848 × 10-7, 2.12437 × 10-7, 2.12036 × 10-7, 2.11646 × 10-7,
2.11266 × 10-7, 2.10896 × 10-7, 2.10535 × 10-7, 2.10183 × 10-7, 2.09839 × 10-7, 2.09504 × 10-7,
2.09177 × 10-7, 2.08858 × 10-7, 2.08546 × 10-7, 2.08241 × 10-7, 2.07944 × 10-7, 2.07653 × 10-7}
```

In[21]:=

```
φOut = fTABLE;
For[n = 1, n < Length[fTABLE] + 1 ,
Part[φOut, n] = (Cos[Part[kξ2LIST, n]]/E^(-Part[κ, n] Part[fTABLE, n]/2))
E^(-Part[κ, n] ξ); n++];
Dimensions[φOut];
```

In[23]:=

```

 $\phi$ Surface =  $\phi$ Out;
For[n = 1, n < Length[tTABLE] + 1 ,
  Part[ $\phi$ Surface, n] = (Cos[Part[k $\xi$ tLIST, n]]/E^(-Part[k, n] Part[tTABLE, n]/2))
  E^(-Part[k, n]Part[tTABLE, n]/2); n++];
 $\phi$ Surface;

```

In[25]:=

```
 $\phi$ In = Cos[k $\xi$ LIST  $\xi$ ];
```

In[26]:=

```

 $\phi$ Out
 $\phi$ In

```

Out[26]=

```

{1.00558 e-0.000979  $\xi$ , 1.00797 e-1.05592*106  $\xi$ , 1.01075 e-1.21756*106  $\xi$ , 1.01389 e-1.37346*106  $\xi$ ,
1.01738 e-1.52235*106  $\xi$ , 1.0212 e-1.66702*106  $\xi$ , 1.02533 e-1.80441*106  $\xi$ , 1.02975 e-1.93554*106  $\xi$ ,
1.03443 e-2.06051*106  $\xi$ , 1.03938 e-2.17946*106  $\xi$ , 1.04456 e-2.2926*106  $\xi$ , 1.04997 e-2.40014*106  $\xi$ ,
1.05559 e-2.50233*106  $\xi$ , 1.06142 e-2.59941*106  $\xi$ , 1.06744 e-2.69165*106  $\xi$ , 1.07365 e-2.7793*106  $\xi$ ,
1.08003 e-2.86261*106  $\xi$ , 1.08658 e-2.94183*106  $\xi$ , 1.09329 e-3.01718*106  $\xi$ , 1.10016 e-3.0889*106  $\xi$ ,
1.10719 e-3.1572*106  $\xi$ , 1.11436 e-3.22228*106  $\xi$ , 1.12167 e-3.28432*106  $\xi$ , 1.12913 e-3.34251*106  $\xi$ ,
1.13672 e-3.40001*106  $\xi$ , 1.14445 e-3.45399*106  $\xi$ , 1.15231 e-3.50558*106  $\xi$ , 1.1603 e-3.55493*106  $\xi$ ,
1.16843 e-3.60217*106  $\xi$ , 1.17668 e-3.64741*106  $\xi$ , 1.18505 e-3.69076*106  $\xi$ , 1.19356 e-3.73234*106  $\xi$ ,
1.20219 e-3.77224*106  $\xi$ , 1.21094 e-3.81055*106  $\xi$ , 1.21982 e-3.84736*106  $\xi$ , 1.22882 e-3.88274*106  $\xi$ ,
1.23794 e-3.91677*106  $\xi$ , 1.24719 e-3.94952*106  $\xi$ , 1.25656 e-3.98107*106  $\xi$ , 1.26606 e-4.01146*106  $\xi$ ,
1.27567 e-4.04075*106  $\xi$ , 1.28542 e-4.06901*106  $\xi$ , 1.29528 e-4.09627*106  $\xi$ , 1.30528 e-4.1226*106  $\xi$ ,
1.31539 e-4.14803*106  $\xi$ , 1.32564 e-4.1726*106  $\xi$ , 1.33601 e-4.19636*106  $\xi$ , 1.3465 e-4.21934*106  $\xi$ ,
1.35713 e-4.24157*106  $\xi$ , 1.36788 e-4.2631*106  $\xi$ , 1.37877 e-4.28395*106  $\xi$ , 1.38978 e-4.30415*106  $\xi$ ,
1.40092 e-4.32273*106  $\xi$ , 1.4122 e-4.34272*106  $\xi$ , 1.42361 e-4.36114*106  $\xi$ , 1.43516 e-4.37901*106  $\xi$ ,
1.44683 e-4.39636*106  $\xi$ , 1.45865 e-4.41321*106  $\xi$ , 1.4706 e-4.42957*106  $\xi$ , 1.4827 e-4.44548*106  $\xi$ ,
1.49493 e-4.46093*106  $\xi$ , 1.5073 e-4.47597*106  $\xi$ , 1.51982 e-4.49059*106  $\xi$ , 1.53247 e-4.50481*106  $\xi$ ,
1.54528 e-4.51866*106  $\xi$ , 1.55823 e-4.53213*106  $\xi$ , 1.57132 e-4.54526*106  $\xi$ , 1.58457 e-4.55804*106  $\xi$ ,
1.59797 e-4.5705*106  $\xi$ , 1.61151 e-4.58264*106  $\xi$ , 1.62521 e-4.59448*106  $\xi$ , 1.63907 e-4.60602*106  $\xi$ ,
1.65308 e-4.61728*106  $\xi$ , 1.66725 e-4.62826*106  $\xi$ , 1.68158 e-4.63898*106  $\xi$ , 1.69607 e-4.64945*106  $\xi$ ,
1.71072 e-4.65966*106  $\xi$ , 1.72554 e-4.66963*106  $\xi$ , 1.74052 e-4.67938*106  $\xi$ , 1.75567 e-4.68889*106  $\xi$ ,
1.77098 e-4.6982*106  $\xi$ , 1.78647 e-4.70729*106  $\xi$ , 1.80213 e-4.71617*106  $\xi$ , 1.81797 e-4.72486*106  $\xi$ ,
1.83398 e-4.73236*106  $\xi$ , 1.85017 e-4.74167*106  $\xi$ , 1.86654 e-4.7498*106  $\xi$ , 1.88309 e-4.75776*106  $\xi$ ,
1.89983 e-4.76555*106  $\xi$ , 1.91675 e-4.77317*106  $\xi$ , 1.93386 e-4.78064*106  $\xi$ , 1.95116 e-4.78795*106  $\xi$ ,
1.96865 e-4.79511*106  $\xi$ , 1.98633 e-4.80212*106  $\xi$ , 2.00421 e-4.80899*106  $\xi$ , 2.02228 e-4.81572*106  $\xi$ }

```

Out[27]=

```
{Cos[8.41758 × 106 ξ], Cos[8.36807 × 106 ξ], Cos[8.31166 × 106 ξ], Cos[8.24922 × 106 ξ],  
Cos[8.18157 × 106 ξ], Cos[8.10954 × 106 ξ], Cos[8.03391 × 106 ξ], Cos[7.95539 × 106 ξ],  
Cos[7.87464 × 106 ξ], Cos[7.79222 × 106 ξ], Cos[7.70866 × 106 ξ], Cos[7.6244 × 106 ξ],  
Cos[7.53983 × 106 ξ], Cos[7.45527 × 106 ξ], Cos[7.371 × 106 ξ], Cos[7.28726 × 106 ξ],  
Cos[7.20422 × 106 ξ], Cos[7.12206 × 106 ξ], Cos[7.04089 × 106 ξ], Cos[6.96082 × 106 ξ],  
Cos[6.88193 × 106 ξ], Cos[6.80428 × 106 ξ], Cos[6.72791 × 106 ξ], Cos[6.65285 × 106 ξ],  
Cos[6.57913 × 106 ξ], Cos[6.50676 × 106 ξ], Cos[6.43574 × 106 ξ], Cos[6.36606 × 106 ξ],  
Cos[6.29772 × 106 ξ], Cos[6.2307 × 106 ξ], Cos[6.165 × 106 ξ], Cos[6.10058 × 106 ξ],  
Cos[6.03743 × 106 ξ], Cos[5.97552 × 106 ξ], Cos[5.91484 × 106 ξ], Cos[5.85535 × 106 ξ],  
Cos[5.79704 × 106 ξ], Cos[5.73986 × 106 ξ], Cos[5.68381 × 106 ξ], Cos[5.62884 × 106 ξ],  
Cos[5.57494 × 106 ξ], Cos[5.52208 × 106 ξ], Cos[5.47023 × 106 ξ], Cos[5.41937 × 106 ξ],  
Cos[5.36947 × 106 ξ], Cos[5.3205 × 106 ξ], Cos[5.27245 × 106 ξ], Cos[5.22529 × 106 ξ],  
Cos[5.17899 × 106 ξ], Cos[5.13354 × 106 ξ], Cos[5.08892 × 106 ξ], Cos[5.04509 × 106 ξ],  
Cos[5.00204 × 106 ξ], Cos[4.95976 × 106 ξ], Cos[4.91821 × 106 ξ], Cos[4.87739 × 106 ξ],  
Cos[4.83727 × 106 ξ], Cos[4.79784 × 106 ξ], Cos[4.75907 × 106 ξ], Cos[4.72096 × 106 ξ],  
Cos[4.68348 × 106 ξ], Cos[4.64662 × 106 ξ], Cos[4.61037 × 106 ξ], Cos[4.57471 × 106 ξ],  
Cos[4.53962 × 106 ξ], Cos[4.50509 × 106 ξ], Cos[4.47111 × 106 ξ], Cos[4.43766 × 106 ξ],  
Cos[4.40474 × 106 ξ], Cos[4.37233 × 106 ξ], Cos[4.34041 × 106 ξ], Cos[4.30898 × 106 ξ],  
Cos[4.27802 × 106 ξ], Cos[4.24753 × 106 ξ], Cos[4.21749 × 106 ξ], Cos[4.18789 × 106 ξ],  
Cos[4.15873 × 106 ξ], Cos[4.12999 × 106 ξ], Cos[4.10166 × 106 ξ], Cos[4.07374 × 106 ξ],  
Cos[4.04621 × 106 ξ], Cos[4.01907 × 106 ξ], Cos[3.99231 × 106 ξ], Cos[3.96593 × 106 ξ],  
Cos[3.9399 × 106 ξ], Cos[3.91423 × 106 ξ], Cos[3.88891 × 106 ξ], Cos[3.86392 × 106 ξ],  
Cos[3.83927 × 106 ξ], Cos[3.81495 × 106 ξ], Cos[3.79095 × 106 ξ], Cos[3.76726 × 106 ξ],  
Cos[3.74388 × 106 ξ], Cos[3.7208 × 106 ξ], Cos[3.69801 × 106 ξ], Cos[3.67552 × 106 ξ]}
```

In[29]:=

```
pp = Table[ξ, {ξ, 0, 3 * 10-6, 5 * 10-9};
```

In[30]:=

```
IntensityOut = Table[0, {t, 1, Length[tTABLE], 1}, {ξ, 0, 3 * 10-6, 5 * 10-9};  
IntensityIn = Table[0, {t, 1, Length[tTABLE], 1}, {ξ, 0, 3 * 10-6, 5 * 10-9};  
LayerMark = Table[0, {t, 1, Length[tTABLE], 1}, {ξ, 0, 3 * 10-6, 5 * 10-9};
```

In[33]:=

```
For[pp = 1, pp < Length[tTABLE] + 1,  
Part[IntensityIn, pp] =  
Table[Which[Part[tTABLE, pp]/2 ≤ ξ < ∞, 0, True, Part[#In, pp]^2],  
{ξ, 0, 3 * 10-6, 5 * 10-9}; pp++];  
Dimensions[IntensityIn]  
IntensityIn;
```

Out[34]=

{96, 601}

In[36]:=

```
For[pp = 1, pp < Length[tTABLE] + 1,
  Part[IntensityOut, pp] =
    Table[Which[Part[tTABLE, pp]/2 ≤ ξ < ∞, Part[ϕOut, pp]^2, True, 0],
      {ξ, 0, 3 * 10^-6, 5 * 10^-9}]; pp++;
Dimensions[IntensityOut]
IntensityOut;
```

Out[37]=

{96, 601}

In[39]:=

```
For[pp = 1, pp < Length[tTABLE] + 1,
  Part[LayerMark, pp] =
    Table[Which[(Part[tTABLE, pp]/2) ≤ ξ < (tINC/2 + Part[tTABLE, pp]/2),
      1, True, 0], {ξ, 0, 3 * 10^-6, 5 * 10^-9}]; pp++;
Dimensions[LayerMark]
LayerMark;
```

Out[40]=

{96, 601}

In[42]:=

```
IntensityAllRight = IntensityOut + IntensityIn (* + LayerMark *);
```

In[43]:=

```
IntensityAllLeft = Transpose[Reverse[Transpose[IntensityAllRight]]];
```

In[44]:=

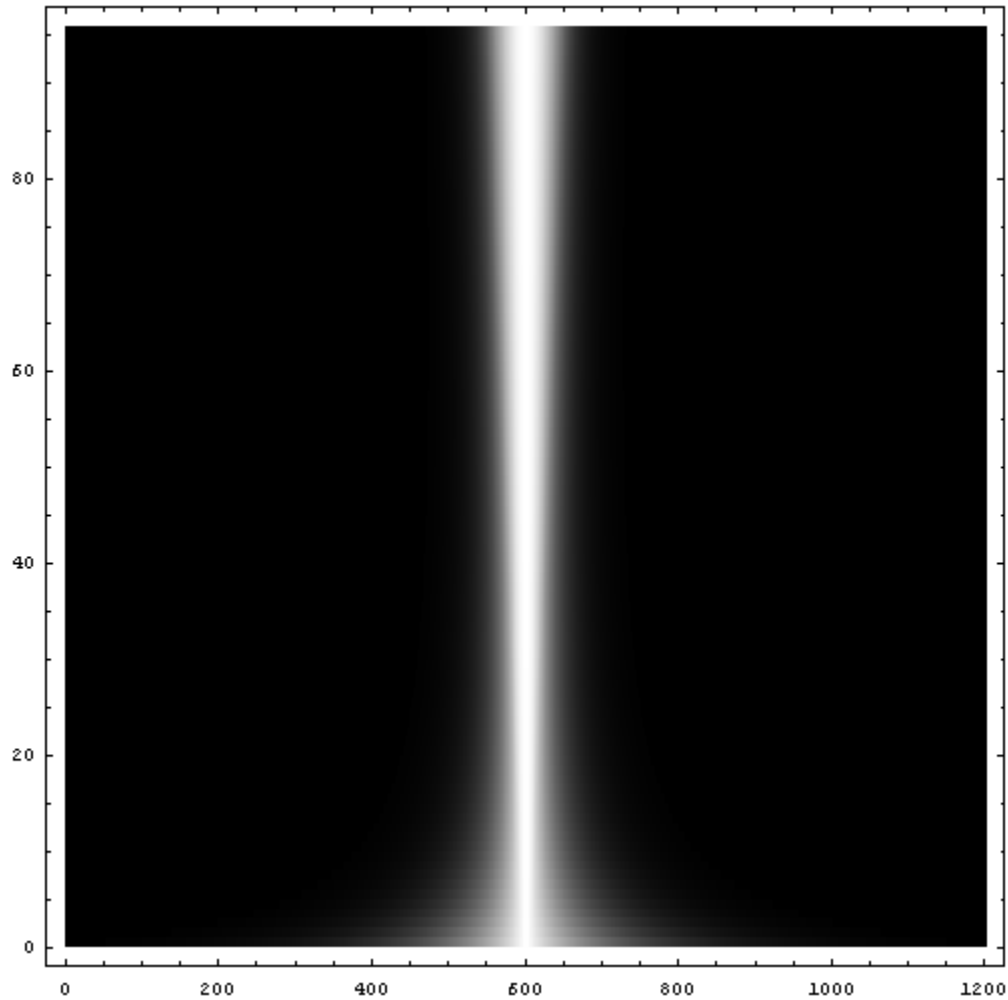
```
IntensityAll =
  Transpose[Join[Transpose[IntensityAllLeft], Transpose[IntensityAllRight]]];
```

In[45]:=

```
Export["IntensityAll_N0mark.dat", IntensityAll, "Table"];
```

In[46]:=

```
IntensityAllPlot = ListDensityPlot[IntensityAll, Mesh -> False,  
(* ColorFunction->(Hue[#]&), *) PlotRange -> All, ImageSize -> 500]
```



In[47]:=

```
zMAX = Sqrt[1 (1 + 1)] / R * tTABLE / 2 * Sqrt[{nR^2 - 1)];  
z = Sqrt[(-1 + Sqrt[(1 + 4 * nR^2 * zMAX^2))] / (2 * nR^2)]  
(*1st order approximation*);
```

In[49]:=

```
a = ListPlot[Transpose[{tTABLE $\mu$ , k&t2LIST}],  
ImageSize -> {500, Automatic}, PlotStyle -> Hue[.9],  
DisplayFunction -> Identity];
```

In[50]:=

```

b = ListPlot[Transpose[{tTABLE $\mu$ , z}],
  ImageSize  $\rightarrow$  {500, Automatic}, PlotStyle  $\rightarrow$  Hue[.6],
  DisplayFunction  $\rightarrow$  Identity];

```

In[51]:=

```

c = ListPlot[{{0, 0}}, DisplayFunction  $\rightarrow$  Identity];

```

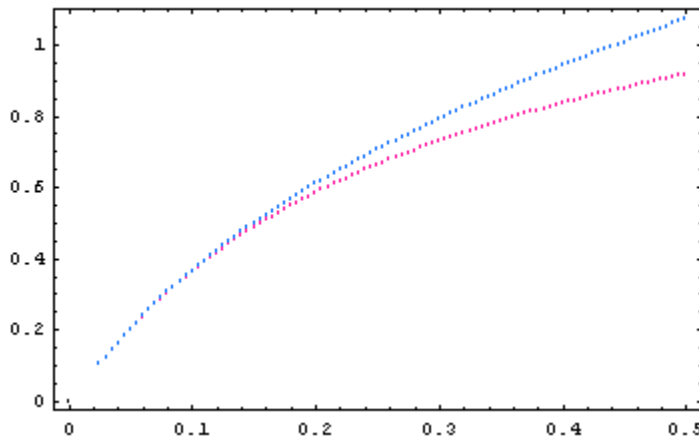
In[52]:=

```

Show[{a, b, c}, AxesOrigin  $\rightarrow$  {0, 0}, Frame  $\rightarrow$  True,
  AxesLabel  $\rightarrow$  {"t (m)", "k $\xi$  t/2 (radians)"},
  PlotLabel  $\rightarrow$ 
    "k $\xi$ t/2 through transcendental (Red) and 1st order
    approximation (Blue)"
  , DisplayFunction  $\rightarrow$  $DisplayFunction,
  ImageSize  $\rightarrow$  {400, Automatic}];

```

z/2 through transcendental (Red) and 1st order approximation (Blue)



(* Estimated Enhancement *)

In[54]:=

```

le = tTABLE / (2 zMAX^2);

```

In[55]:=

```

Enhancement1 = (nLayer^2 - 1) * R /
  (nLayer^2 * tTABLE (Sec[ $\gamma$ ]^2 + Tan[ $\gamma$ ] /  $\gamma$ ) + 2 *  $\Gamma$ )
EnhancementM1 = Transpose[{tTABLE $\mu$ , Enhancement1}];
E01 = ListPlot[EnhancementM1, AxesOrigin  $\rightarrow$  {0, 0},
  PlotStyle  $\rightarrow$  Hue[.9], DisplayFunction  $\rightarrow$  Identity];

```

Out[55]=

```
{65.5814, 76.1231, 85.5083, 93.7085, 100.736, 106.635, 111.473, 115.335, 118.311, 120.495,
121.981, 122.856, 123.204, 123.1, 122.611, 121.798, 120.715, 119.408, 117.919, 116.281,
114.526, 112.679, 110.763, 108.796, 106.795, 104.772, 102.74, 100.707, 98.6824, 96.6716,
94.6806, 92.7138, 90.7747, 88.8662, 86.9907, 85.1498, 83.345, 81.5771, 79.8467, 78.1544,
76.5001, 74.8839, 73.3055, 71.7647, 70.261, 68.7939, 67.3629, 65.9672, 64.6062, 63.2792,
61.9855, 60.7243, 59.4947, 58.2962, 57.1278, 55.9888, 54.8785, 53.7961, 52.7407, 51.7118,
50.7086, 49.7303, 48.7763, 47.8458, 46.9383, 46.0531, 45.1895, 44.3469, 43.5247,
42.7225, 41.9395, 41.1752, 40.4291, 39.7008, 38.9896, 38.2951, 37.6169, 36.9545,
36.3073, 35.6751, 35.0574, 34.4537, 33.8638, 33.2871, 32.7234, 32.1724, 31.6335,
31.1066, 30.5912, 30.0872, 29.5941, 29.1117, 28.6397, 28.1778, 27.7258, 27.2834}
```

In[58]:=

```
Enhancement1b =  
( (nLayer^2 - 1) * R ) /  
(nLayer^2 * tTABLE (Sec[z]^2 + Tan[z] / z) + 2 * Γ);  
EnhancementM1b = Transpose[{tTABLEμ, Enhancement1b}];  
E01b = ListPlot[EnhancementM1b, AxesOrigin -> {0, 0},  
PlotStyle -> Hue[.75], DisplayFunction -> Identity];
```

In[61]:=

```
Enhancement2 = ( (nLayer^2 - 1) * R ) /  
(nLayer^2 * tTABLE (Sec[z]^2 + Tan[z] / z) + tTABLE / (zMAX)^2)  
EnhancementM2 = Transpose[{tTABLEμ, Enhancement2}];  
E02 = ListPlot[EnhancementM2, AxesOrigin -> {0, 0},  
PlotStyle -> Hue[.6], DisplayFunction -> Identity];
```

Out[61]=

```
{67.1148, 78.5993, 89.1468, 98.689, 107.187, 114.628, 121.025, 126.409, 130.828, 134.342,
137.019, 138.931, 140.153, 140.758, 140.819, 140.403, 139.573, 138.388, 136.902,
135.162, 133.212, 131.09, 128.829, 126.459, 124.005, 121.491, 118.934, 116.351, 113.757,
111.162, 108.578, 106.013, 103.473, 100.964, 98.4912, 96.0579, 93.6673, 91.3216,
89.0226, 86.7715, 84.5692, 82.4162, 80.3126, 78.2584, 76.2533, 74.297, 72.3887, 70.528,
68.7138, 66.9455, 65.2222, 63.5427, 61.9063, 60.3118, 58.7583, 57.2447, 55.77, 54.3332,
52.9333, 51.5694, 50.2403, 48.9452, 47.6831, 46.4531, 45.2542, 44.0857, 42.9466,
41.8362, 40.7535, 39.6979, 38.6686, 37.6647, 36.6857, 35.7307, 34.7992, 33.8905,
33.0039, 32.1388, 31.2947, 30.4709, 29.667, 28.8823, 28.1164, 27.3687, 26.6388, 25.9262,
25.2305, 24.5511, 23.8878, 23.24, 22.6073, 21.9895, 21.3861, 20.7967, 20.2211, 19.6588}
```

In[64]:=

```

e012 = (Enhancement1 - Enhancement2) / Enhancement1 * 100;
e012M = Transpose[{tTABLEμ, e012}];
e012P = ListPlot[e012M, AxesOrigin → {0, 0},
  PlotStyle → Hue[.25], DisplayFunction → Identity];

```

In[67]:=

```

e011b = (Enhancement1 - Enhancement1b) / Enhancement1 * 100;
e011bM = Transpose[{tTABLEμ, e011b}];
e011bP = ListPlot[e011bM, AxesOrigin → {0, 0},
  PlotStyle → Hue[.4], DisplayFunction → Identity];

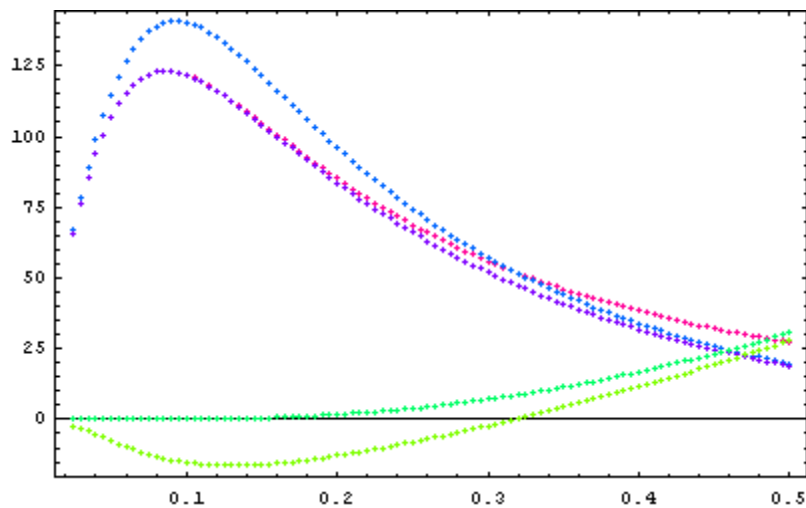
```

In[70]:=

```

Show[{E01, E02, E01b, e011bP, e012P}, Frame → True,
  AxesOrigin → {0, 0}, DisplayFunction → $DisplayFunction,
  ImageSize → {400, Automatic}, PlotRange → All]

```



In[71]:=

```

e012M = Transpose[{tTABLEμ, e012}];
e012P = ListPlot[e012M, AxesOrigin → {0, 0},
  PlotStyle → Hue[.4], DisplayFunction → Identity];

```

In[73]:=

```

IM = Transpose[{tTABLEμ, Γ}];
b01 = ListPlot[IM, AxesOrigin → {0, 0}, PlotStyle → Hue[.9],
  DisplayFunction → Identity];

```

In[75]:=

```

x01 = Transpose[{tTABLEμ, x}];
m01 = ListPlot[x01, AxesOrigin → {0, 0}, PlotStyle → Hue[.9],
  DisplayFunction → Identity];

```

In[77]:=

```

leM = Transpose[{tTABLEμ, le}];
b02 = ListPlot[leM, AxesOrigin → {0, 0}, PlotStyle → Hue[.6],
  DisplayFunction → Identity];

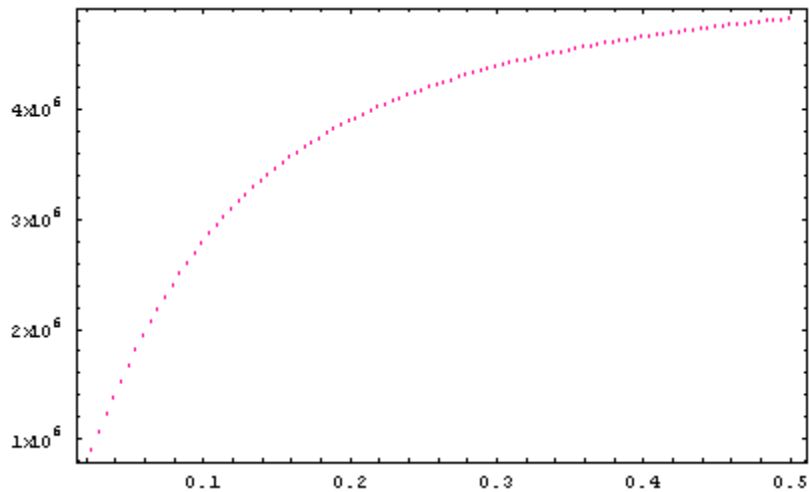
```

In[79]:=

```

Show[{m01}, Frame → True, AxesOrigin → {0, 0},
  DisplayFunction → $DisplayFunction,
  ImageSize → {400, Automatic}, PlotRange → All ]

```



In[80]:=

```

nt = nLayer^2 * tTABLE (Sec[γ]^2 + Tan[γ] / γ);
ntM = Transpose[{tTABLEμ, nt}];
a01 = ListPlot[ntM, AxesOrigin → {0, 0}, PlotStyle → Hue[.9],
  DisplayFunction → Identity];

```

In[83]:=

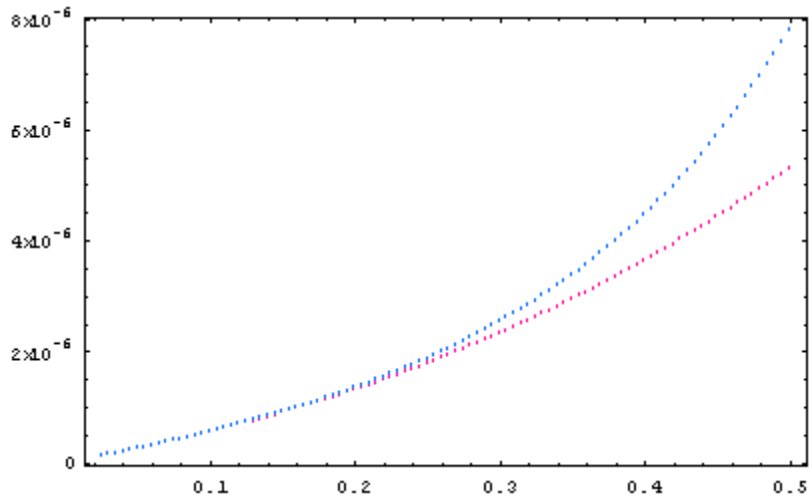
```

nt2 = nLayer^2 * tTABLE (Sec[z]^2 + Tan[z] / z);
nt2M = Transpose[{tTABLEμ, nt2}];
a02 = ListPlot[nt2M, AxesOrigin → {0, 0}, PlotStyle → Hue[.6],
  DisplayFunction → Identity];

```

In[86]:=

```
Show[{a01, a02}, Frame → True, AxesOrigin → {0, 0},
      DisplayFunction → $DisplayFunction,
      ImageSize → {400, Automatic}, PlotRange → All ]
```



In[87]:=

```
(*          asymptotes
      *)
```

In[88]:=

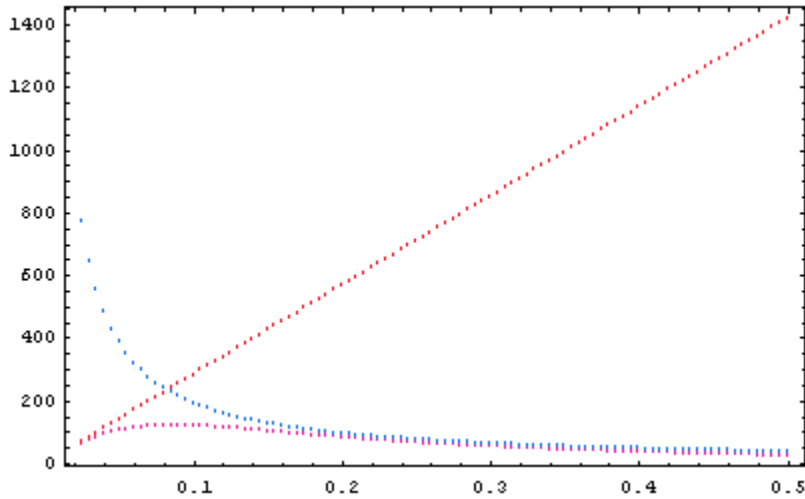
```
asymptote1 = (nLayer^2 - nOut^2) * R / (Pi * nLayer^2 * tTABLE);
asymptote1M = Transpose[{tTABLEμ, asymptote1}];
A01 = ListPlot[asymptote1M, AxesOrigin → {0, 0},
               PlotStyle → Hue[.6], DisplayFunction → Identity];
```

In[91]:=

```
asymptote2 = (nLayer^2 - nOut^2) * R / (nOut^2 * tTABLE / (zMAX)^2);
asymptote2M = Transpose[{tTABLEμ, asymptote2}];
A02 = ListPlot[asymptote2M, AxesOrigin → {0, 0},
               PlotStyle → Hue[.99], DisplayFunction → Identity];
```

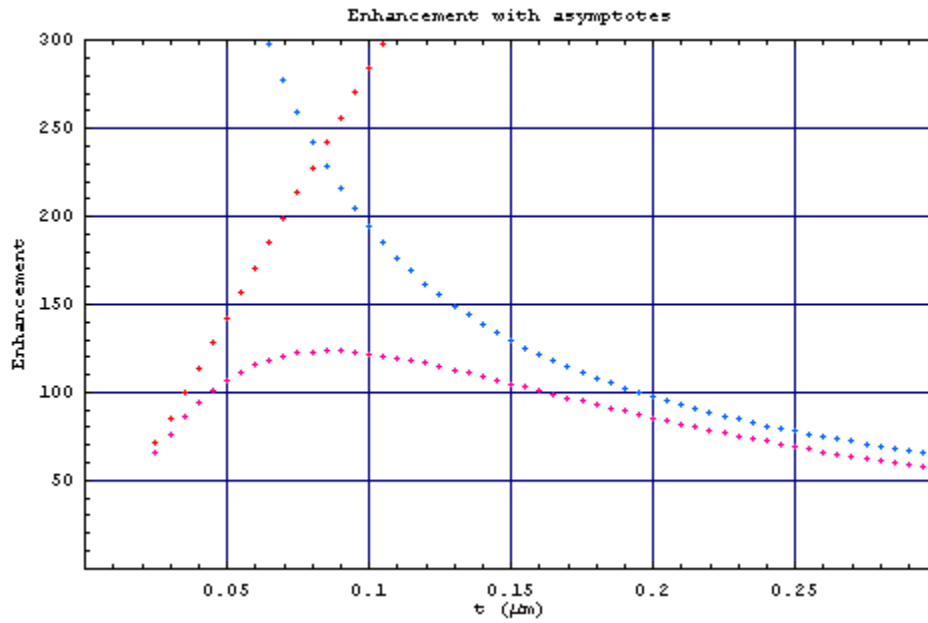
In[94]:=

```
Show[{E01, A01, A02}, Frame → True, AxesOrigin → {0, 0},
      DisplayFunction → $DisplayFunction,
      ImageSize → {400, Automatic}, PlotRange → All ]
```



In[95]:=

```
Show[{ E01, A01, A02}, Frame → True , AxesOrigin → {0, 0},
  DisplayFunction → $DisplayFunction,
  ImageSize → {500, Automatic}, PlotRange → {{0, 0.3}, {0, 300}},
  FrameLabel → {"t (μm)", "Enhancement"},
  "Enhancement with asymptotes", ""}, GridLines → Automatic]
```



SPECTROSCOPY OF PHOTONIC ATOMS: A MEANS FOR ULTRA-SENSITIVE SPECIFIC SENSING OF BIO-MOLECULES

STEPHEN ARNOLD and OPHIR GAATHON

*Microparticle Photophysics Laboratory(MP³L)
Polytechnic University, Brooklyn, N.Y. 11201*

Abstract

By combining bio-recognition using bio-nano-sensors with the transduction capability of resonant dielectric micro-cavities, we demonstrate the specific identification of protein and DNA. This is accomplished through the spectroscopy of a microcavity as molecular adsorption takes place on its functionalized surface. A surprising aspect is that this sensing paradigm is not only ultra-sensitive but also provides a measure of molecular weight and the thickness of molecular monolayers on the microcavity surface.

1. Introduction

The specific detection and measurement of the concentration of biological entities (e.g. protein, DNA, virus) is important since the appearance of specific bio-molecules can alter our lives for better and worse. An optical approach to this task is what this paper is all about. It fits into a new area, Bio-Photonics, for which there is much current activity.¹

One must first realize that most bio-molecules (e.g. protein, DNA) fall into the nanoscopic realm. For example, in our blood a particular protein, Human Serum Albumin (HSA) is prominent. It is about 3 nm in size, however with a molecular weight of 66,438 (also specified as 66.438 kDa) it contains a vast multitude of vibrational modes, principally associated with 20 amino acids. Since virtually all protein molecules contain these same amino acids (constructed in different sequences), the IR spectra from one protein to the other are virtually the same. Biology runs itself on these proteins. Each of the approx. 30,000 genes within our nuclear DNA encode for a separate protein. They are biologically distinguishable, but optically very similar. Faced with this difficulty an optical specialist has to rethink the means by which to identify a given protein. Some years ago our laboratory came to a painful conclusion. Molecular spectroscopy is an unlikely candidate!

To understand how to proceed we attempted to learn from nature. There are all sorts of ways in which nature can make light, but there is no light inside our bodies. Yet our bodies recognize tens of thousands of different proteins well enough to enable us to function. Biological interaction involves multiple unique chemical bonding. Each type of interaction involves complementary molecular structure from all bodies involved. In essence it is no different than the key to lock match (but on a much smaller scale). For example in a sensitized person, the allergic reaction to certain toxic proteins on the surface of a pollen grain causes a specific antibody to engulf the invading allergen like a lock covering a key. This highly specific physio-chemical recognition will not occur with other proteins. Another example is the hybridization that occurs between complimentary strands of DNA. If we mimic biology, we would also sense bio-molecules through these “dark interactions”, rather than looking for changes in the molecular spectrum. The trick is to distribute a variety of distinguishable locks on separate transducers and sensitively determine onto which lock the key attaches.

As a transducer we have chosen a resonant dielectric microcavity whose state functions resemble those of a hydrogen atom. This “photonic atom” will be found to shift the frequency of its resonant modes by the surface adsorption of a few bio-molecules.^{2,3}

In what follows we first describe the photonic atom (PA) descriptively followed by some of its more detailed physics. Following this we discuss the sensitivity of the PA to molecular adsorption. Finally we describe specific detection schemes for protein and DNA without labels.

2. Photonic Atom

Photonic Atoms are dielectric microspheres that demonstrate high Q resonances associated with Whispering Gallery Modes (WGMs).

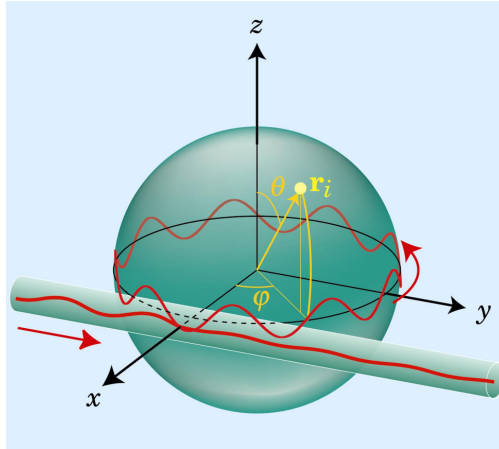


Fig.1 Illustration of coupling of optical energy between a guided wave in a tapered optical fiber and a Photonic Atom mode in a microsphere.⁴ The vector \mathbf{r}_i points to a small nano-perturbation.

A high Q resonance is one with a very narrow linewidth in frequency δf ; $\delta f = f / Q$. From a geometrical point of view light is confined within the microsphere by total internal reflection (TIR) against the inner surface. As with all systems that confine light by TIR an exponentially decaying evanescent field extends just beyond (~ 200 nm) the sphere radius ($\sim 100\mu\text{m}$). It is this field which allows the resonant mode to be influenced from the outside. Fig. 1 shows the wave point of view. When light circumnavigates the sphere and returns in phase the system is resonant. Here evanescent coupling to a guided wave in a tapered optical fiber (dia. $4\mu\text{m}$) stimulates the mode, leading to a dip in the transmission spectrum through the fiber.⁵ The wave circumnavigating the sphere is reminiscent of a *de Broglie matter wave* circling the electron orbit in a Bohr atom. Indeed the detailed description of this atomic system is similar to the description of the photon orbit in the dielectric sphere (Fig.1).

In hydrogen the electron orbits are distinguished by the parameter set v, l, m, s representing the principle (radial) quantum number, the angular momentum quantum number, the azimuthal quantum number (z-projection of angular momentum), and the spin quantum number, respectively. In the photonic atom the first three are still used, but the spin quantum number is replaced with the polarization state of the orbit, which we will designate as P. As in the case of the spin, P has two values designated as TE for transverse electric and TM for transverse magnetic. The simple wave depicted in Fig.1 is transverse electric with the electric field oscillating tangent to the surface. The electric field of a TM resonance oscillates in the plane of the orbit. One can specifically select TE or TM modes by polarizing light in the coupling fiber either tangent or perpendicular to the surface of the microsphere, respectively. We will designate a particular mode by P_{lm}^v . The mode in Fig.1 happens to be equatorial with its angular momentum directed along the z-axis. For such a mode $l = m$. The designation for this particular mode is $\text{TE}_{13,13}^1$.

Each photonic atom mode occurs at a specific optical frequency. However, since these frequencies are sensitive to the circumference of the orbit even a nanoscopic particle adsorbed on the surface can shift this frequency. This frequency shift provides the transduction principle for the Photonic Atom Bio-sensor.

3. Photonic Atom Physics: Hueristics

To understand the sensitivity of a Photonic Atom mode to perturbation we take a heuristic approach. Consider a mode in the equatorial plane (Fig.2a) and imagine that we add a layer of identical material to the surface of the microsphere (Fig.2b).

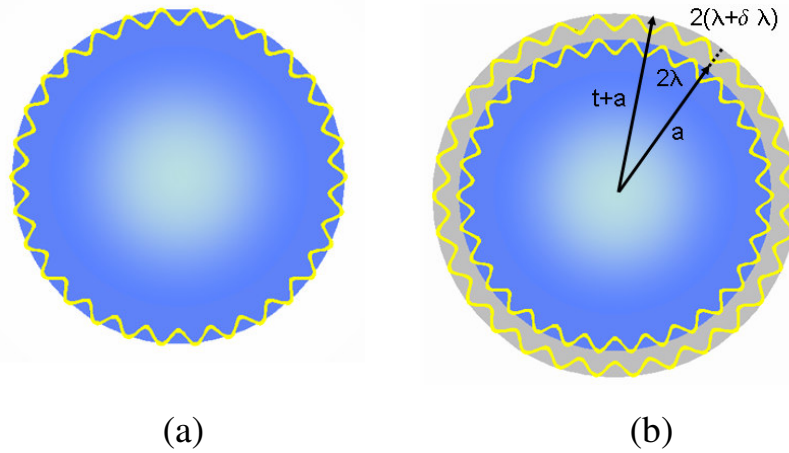


Fig.2 (a) Photonic Atom Mode; (b) Anticipated wavelength change caused by the addition of a spherically symmetric layer.

To maintain the same mode l must be invariant. This scales the whole problem up and as a consequence the wavelength within the mode is changed in proportion to the thickness of the layer. On this basis the fractional increase in wavelength $\delta\lambda/\lambda$ will be approximately equal to the fractional increase in radius t/a ,

$$\frac{\delta\lambda}{\lambda} \approx \frac{t}{a}. \quad (1)$$

Suppose now that the adsorbing material is 1.0 nanometer in thickness. For a sphere having a 100 μm radius, the fractional shift in wavelength according to Eqn.1 would be $\sim 10^{-5}$. This is smaller than the resolution of a grating spectrometer, but is a “piece of cake” (i.e. easy) for the microsphere as a spectrometer. The reason is that the resonances of a microsphere are extremely narrow. Resonances with Q’s of 10^7 (linewidth of 1 part in 10^7) are considered “broad”.⁶ But such a “broad” line would shift 100 times its linewidth for a 1.0 nm layer. For it to shift just one linewidth requires only

a 10 picometer layer (i.e. one tenth the size of a hydrogen atom). So such a small perturbation should be easy to observe. In fact, it is not difficult to define a resonance position to $1/50^{\text{th}}$ of a linewidth, which allows for the observation of a small fraction of a monolayer.

One should doubt Eqn.1. Although it is heuristically appealing, it is limited. After all, adsorbed bio-molecules most likely don't have the same dielectric properties as the glass we will ultimately use for our microcavity. In addition, we have clearly simplified the properties of the modes. Further understanding can only be obtained from a solution for $\delta\lambda/\lambda$ from Maxwell's equations.

4. Photonic Atom Physics 101

A meaningful attempt to obtain an exact solution to the problem of layer perturbation was described within the proceedings of the previous school.⁷ That work has been extended. Herein we will describe the method of calculation in brief, and report the major result.

Our approach relies on a quantum analog of the electrodynamic problem. It is our belief that exposure to quantum mechanics is more ubiquitous to the sciences (e.g. Physics, Chemistry, and Biology) than electromagnetics. So where it is possible we reduce the vector time-harmonic electromagnetic problem to a scalar quantum analog. This is not particularly difficult in the case of the spherical dielectric cavity since as we have already pointed out there are similarities between this problem and the atomic problem.

As a first step we must solve the source free vector Helmholtz equation,

$$\nabla^2 \mathbf{E} + k^2 \mathbf{E} = 0. \quad (2)$$

We are particularly interested in modes for which the field and its derivative are continuous at the boundary, just as the wave function would be in quantum mechanics. Of course we would also like to reduce Eqn.1 to a scalar equation. There is a simple choice. We construct the field as the angular momentum operator acting on a scalar function, $\mathbf{E} = \hat{L}\psi$. Since the angular momentum operator has only angular components \mathbf{E} will be tangent at the microsphere surface. With this choice for the field the problem of solving the vector wave equation is easily reduced to the solution of a Schrödinger-like equation for $\psi_r = r\psi$.⁸ The effective energy E_{eff} for this quantum analog is the square of the free space wave vector; $E_{\text{eff}} = k_0^2$, and the effective potential $V_{\text{eff}} = k_0^2(1 - n^2) + l(l+1)/r^2$, where n is the radial refractive index profile, and l is the angular momentum quantum number of a particular mode. A layer perturbation corresponds to changing n^2 from the surface out to a thickness t by $\delta(n^2)$. The first order perturbation has an identical form as we are use to in quantum mechanics,

$$\delta E_{\text{eff}} \approx \langle \psi_r | \delta V_{\text{eff}} | \psi_r \rangle, \quad (3)$$

where ψ_r is constructed from the appropriate quasi-normalized functions.⁹ After substituting for the major components in Eqn. 1 we find that the fractional perturbation in the effective energy is

$$\frac{\delta(k_0^2)}{k_0^2} = -2 \frac{\delta\lambda}{\lambda} = - \left[\frac{2t}{a} \left(\frac{\delta(n^2)}{n_s^2 - n_m^2} \right) \right] \times \left[\frac{L}{t} (1 - e^{-t/L}) \right] \quad (2)$$

where n_s , and n_m are the refractive indices of the sphere (silica, 1.47), and its environment (water, 1.33), respectively, a is the sphere radius, and L is the evanescent field length for grazing incidence; $L = (\lambda/4\pi)(n_{\text{eff}}^2 - n_m^2)^{-1/2}$. If we allow $t/L \ll 1$ and the dielectric constant to be the same as the sphere, Eqn.2 reduces to $\delta\lambda/\lambda \approx t/a$. Aside from being consistent with our heuristic thinking (Eqn.1), Eqn.2 has an interesting structure which allows us to anticipate a number of measurement possibilities in relation to bio-layers.

5. Photonic Atom Sensor as a Nanoscopic Ruler¹⁰

First it should be possible to measure not only the thickness of a nanolayer, but also its excess dielectric constant, simply by obtaining the wavelength shifts of two separate resonance in the same sphere and at the same time. This is because Eqn.2 has a particularly simple structure when one considers that the principle wavelength dependence is contained within the evanescent field length in the rightmost factor on the right hand side. By a judicious choice of the wavelength regions to be used, the leftmost factor on the right hand side can be considered relatively constant. Consequently, by taking a ratio of the fractional shift at one wavelength λ_1 to that at a longer wavelength λ_2 , we arrive at a particularly simple expression that provides the design principle for this surface analysis technique. This ratio S is

$$S = \frac{\left(\frac{\delta\lambda}{\lambda} \right)_1}{\left(\frac{\delta\lambda}{\lambda} \right)_2} \approx \frac{L_1 [1 - e^{-t/L_1}]}{L_2 [1 - e^{-t/L_2}]} \quad (3)$$

For an ultra thin layer (i.e $t/L_1, t/L_2 \ll 1$) S approaches 1, whereas for a thick layer (i.e $t/L_1, t/L_2 \gg 1$) S approaches L_1/L_2 , which with n_{eff} taken constant is just λ_1/λ_2 . For our experiments this ratio is (760nm/1310nm) = 0.58. For these chosen wavelengths S falls off in an approximate exponential fashion in between the two extreme cases with a characteristic length of $t_c = 192$ nm [i.e. $S \approx (L_1/L_2) + (1 - L_1/L_2)\exp(-t/t_c)$]. Measuring S therefore allows us to estimate t . With t in hand, Eqn. 2 gives the excess dielectric constant of the layer, $\delta(n^2)$.

We have performed wavelength multiplexing experiments while forming nano-layers on a silica microsphere surface. Light from two current tunable distributed feed-back (DFB) lasers with nominal wavelengths of 760 nm and 1310 nm was coupled to a single mode fiber (Nufern 780-HP)(Fig. 3). A portion of the fiber was tapered down to

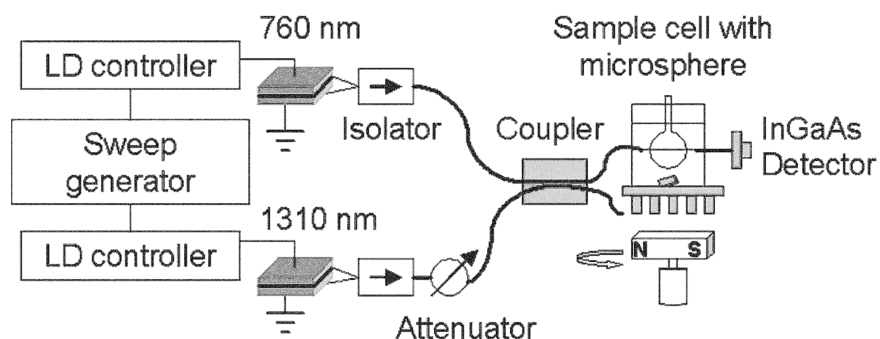


Fig. 3 Experimental setup for wavelength multiplexing of a micro-cavity.¹⁰

3 μm diameter by acid erosion to facilitate coupling to WGMs of a silica microsphere approx. 350 μm in diameter.¹¹ The microsphere and fiber were contained within a temperature controlled 1ml cuvette containing buffer solution and a magnetic stirrer. Beyond this cuvette the fiber was led to an InGaAs detector. By scanning both lasers with a synchronous ramp we observe that the light from each independently stimulates WGMs in the microsphere and gives a distinct transmission spectrum with a superposition of resonant dips from each. By observing which resonances disappear as either laser is shut off, the resonances are easily associated with the 760 nm and 1310 nm region. In this way resonances can be identified and tracked.

As a test of our perturbation theory we constructed two experiments at the extreme limits. First we built a monolayer of a protein (Bovine Serum Albumin, BSA) much thinner (3nm) than the evanescent field length ($\sim 100\text{nm}$).^{4,12} Fig.4 shows a record of the data in real time. The individual curves are typical, and clearly show little difference in the overall shift. In a separate experiment, we added an infinite layer thickness perturbation by increasing the refractive index of the surrounding medium (water) by adding NaCl. In each case the shifts of resonances centered about two wavelengths, $\lambda_1 = 760 \text{ nm}$ and $\lambda_2 = 1310 \text{ nm}$ were measured. These shift are plotted against each other in Fig.5. In a separate experiment, we added an infinite layer thickness perturbation by increasing the refractive index of the surrounding medium (water) by adding NaCl. In each case the shifts of resonances centered about two wavelengths, $\lambda_1 = 760 \text{ nm}$ and $\lambda_2 = 1310 \text{ nm}$ were measured. These shift are plotted against each other in Fig.4. For BSA adsorption S was measured to be 1.04, which compares well with the $t/L \ll 1$ limit for Eqn.3 of 1.00. For the NaCl experiment, S

was measured to be 0.54 whereas the $t/L \gg 1$ limit of Eqn.3 corresponds to $S = 0.58$. This good agreement tests the wavelength dependence of our shift equation and allows the technique to be used as a nanoscopic ruler.

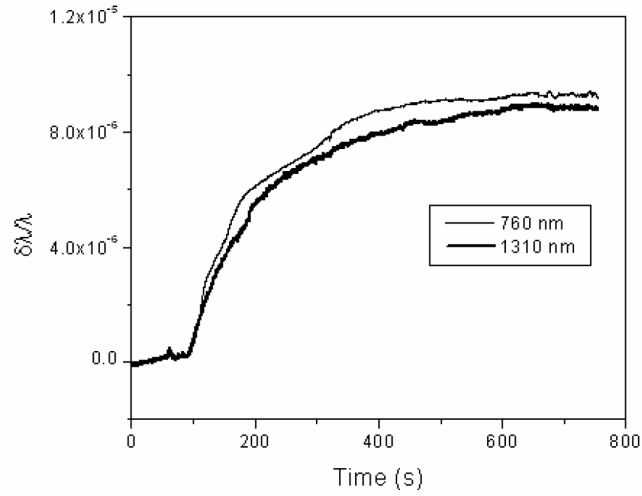


Fig. 4 Resonances shifts at two wavelength [$\lambda_1 = 760$ nm (thin) and $\lambda_2 = 1310$ nm (bold)] due to BSA adsorption.¹⁰

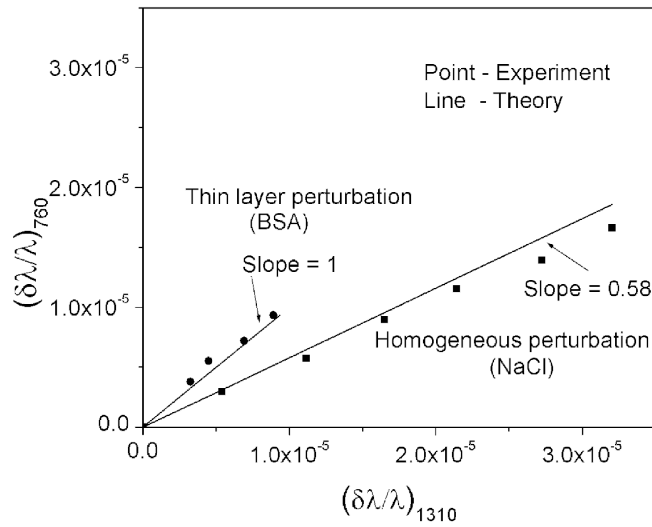


Fig. 5 The plot of $(\delta\lambda/\lambda)_{760 \text{ nm}}$ against $(\delta\lambda/\lambda)_{1310 \text{ nm}}$ for BSA layer and NaCl addition. The lines are the result of layer perturbation theory.¹⁰

In addition upon the determination of t using the multiplexing experiment and Eqn.3, the result can be funneled back into Eqn.2 for the determination of the $\delta(n^2)$ perturbation. For the NaCl solutions the relationship between concentration and the refractive index increment is well documented. By using these tables, the δn arrived at from salt shift measurements enabled us to back out the salt concentration. Concentrations measured in this way were found to be within 3% of the injected concentrations. The challenge is to use this approach to determine the thickness and δn of a dilute soft condensed layer of intermediate thickness.

Poly-L-lysine (PLL) is a polymer that sticks to silica at biological pH (7.2), and takes on an extreme positive charge in water. Consequently PLL is favored as a means for adsorbing bio-molecules with negative charge. However the physical properties of PLL are difficult to measure since it deposits in a thin layer with an extremely low contrast in a water environment. We used a PLL solution from Sigma (P8920, 0.1% w/v in water, the average molecular weigh 225,000 g/mol), which is commonly used in biology to treat glass slides. To generate a layer, 40 μ l of the PLL solution was injected into 900 μ l of PBS surrounding the microsphere. We observed a shift toward longer wavelength that saturated in the usual Langmuir fashion¹³ for monolayer formation. However, the fractional shift at saturation $\sim 2 \times 10^{-6}$ was well below anything we had seen previously. The slope S based on the average of a number of experiments was 0.82. The slope fed back into Eqn. 3 gives a thickness of approximately 110 nm, which is reasonable considering the molecular structure of the polymer. After substituting this thickness into Eqn. 2, we determined the water excess increment in optical dielectric constant to be $\delta(n^2) = 0.0033$. Consequently, $\delta n = 0.0012$, which is indeed small.

6. Protein Molecular Weight Sensitivity of a Photonic Atom Sensor¹⁴

Water-soluble protein molecules are 1-10 nm in size, considerable less than the length of the evanescent field. With this restricted dimension Eqn.2 can be reduced to an approximate form

$$\frac{\delta\lambda}{\lambda} = \frac{t}{a} \left(\frac{\delta(n^2)}{n_s^2 - n_m^2} \right) \quad (4)$$

Eqn.4 suggests that we can normalize data for equatorial radius variations from one microsphere to another by plotting the shift as $(a\delta\lambda/\lambda)$. We see from Eqn.4 that this normalized shift is simply proportional to the thickness of the layer. This suggests that protein with differing molecular weight may give different normalized shifts. Based on this reasoning we carried out a number of experiments in which we adsorbed protein molecules with molecular weights ranging over more than two orders of magnitude. For each molecule a saturation shift was established by varying the concentration in solution until the saturated shift plateaus. Fig. 6 shows each of these so-called isotherms. Indeed the larger molecular weight species show the largest overall shifts.

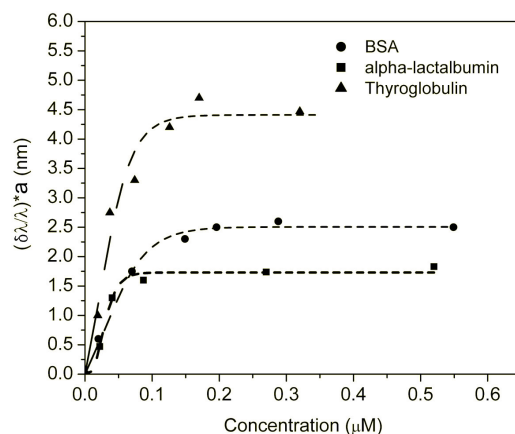


Fig.6 Adsorption isotherms of protein: α -Lactalbumin, BSA and Thyroglobulin with molecular weight of 14.3 kDa, 66 kDa and 670 kDa respectively. The dotted lines are to guide your eyes.¹⁴

Fig.7 is a compendium of the isotherms plateaus for various molecular weights MW. As one can see there is a definite power law behavior. The shift is proportional to $MW^{1/3}$. Considering that globular protein have almost identical densities and dielectric properties due to their common components (i.e. amino acids), $\delta(n^2)$ can be expected to

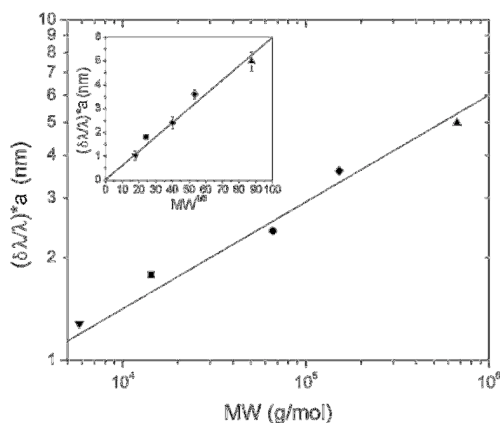


Fig.7 Resonance wavelength shift vs. MW. Form lowest to highest: Insulin, α -Lactalbumin, BSA, γ -Globulin, and Thyroglobulin. The line was drawn manually to fit the data points. Inset: $(\delta\lambda/\lambda)*a$ against $MW^{1/3}$.¹⁴

be nearly constant at saturation. Under these circumstances t dominates the shift. With the protein volume proportional to the molecular weight, the thickness would be expected to be proportional to the cube root of the molecular wt. The small scatter of the points around the $MW^{1/3}$ dependence is surprising considering that protein have

different shapes from one to another. It may well be that protein deformation on adsorption plays a pivotal role in allowing this simple dependence.

7. Specific Detection of Protein ¹²

Up until now we have considered protein adsorbed on a silica surface. There are a number of ways in which this can be facilitated. One means is to functionalize the silica surface with an agent such as 3-aminopropyltriethoxysilane (APTES). This compound reacts with the silanol groups on the silica surface and at biological pH leaves an exposed NH_3^+ group. This is ideal for a protein that acquires a negative charge at this pH; the charge attraction holds the protein in place. Many proteins acquire a net negative charge. So the attachment to the surface is not specific.

To make the attachment specific requires the lock and key relationship that we spoke about earlier. A graphic example can be illustrated in the case of BSA. By chemically attaching biotin (vitamin H) to BSA we generate a modified protein with one major suitor. This so-called biotinylated BSA attaches with one of the strongest known physicochemical bonds to a protein known as streptavidin. Fig.8 pictorially shows the hypothetical configuration.

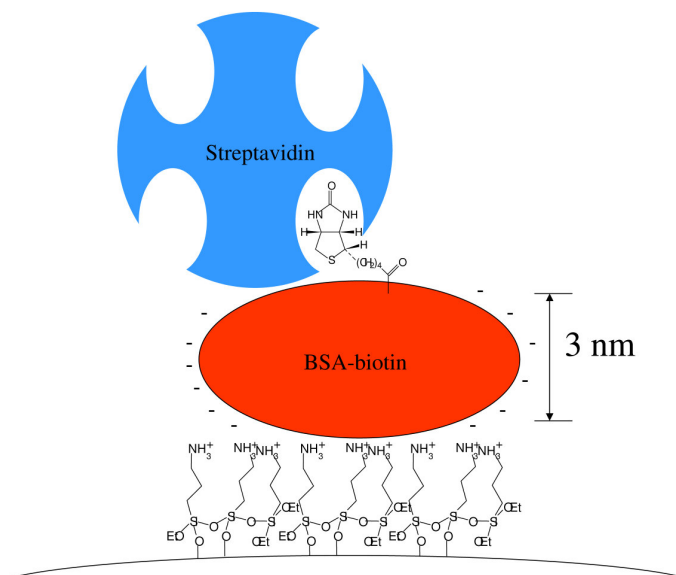


Fig. 8. Biotinylated BSA adsorbed on a functionalized silica surface and “locked” to Streptavidin.

Recall that a typical BSA adsorption experiment on a NH_3^+ group is shown in Fig.4. This experiment was carried out at $1\mu\text{M}$ concentration. As the concentration is increased no additional shift is seen, indicating that the shift is associated with a full monolayer. Apparently the protein is more electrostatically interested in the surface

than other BSA. The same effect occurs with BSA-biotin, however when streptavidin is introduced a pronounced increase in signal is registered (Fig.9). Only streptavidin demonstrates this effect. In addition the increase in signal associated with the streptavidin is only slightly smaller than the BSA signal, consistent with its slightly smaller molecular weight (based on 1:1 stoichiometry for the binding event.).

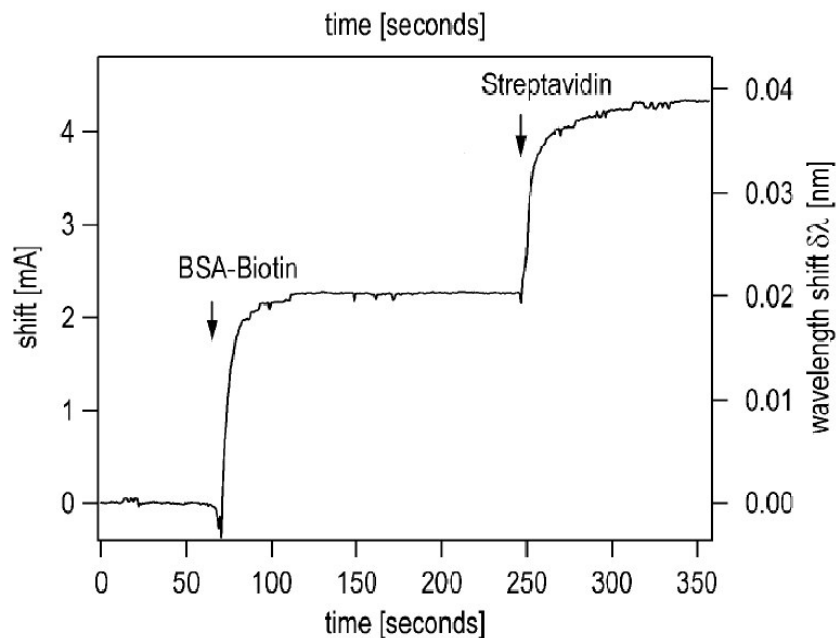


Fig.9. Detection of streptavidin binding to previously surface immobilized BSA biotin.¹²

8. Discrimination of Single Nucleotide Polymorphisms in DNA¹⁵

In 1953 a revolution began in molecular biology with the discovery of the structure of DNA by Crick and Watson.¹⁶ They provided a mechanism for genetic replication (information transfer) and opened the door for the interpretation of nucleotide sequences. With the full genome sequences for a number of species revealed over the past few years, we are now at the beginning of a revolution in genetic analysis.

A major interest is in detecting single defects in DNA (a.k.a. single nucleotide polymorphisms, SNP). SNPs typically occur in fewer than 1 in 1000 bases and are being widely used to better understand disease processes, thereby paving the way for genetic-based diagnostics and therapeutics. Our goal in this section is to understand how our bio-sensor can be used to reveal an SNP. The bio-nano-probe in this case is not a modified protein such as biotinylated BSA, but a complimentary single strand of DNA.

Complimentarity as it is applied to DNA has to do with associations between individual molecules on separate strands. The molecular units, known as bases, are distinguished by the letters A, G, C, and T. The rules are simple: A associates with T

and G associates with C. To understand whether you have a particular stand of DNA a compliment to that strand can be immobilized near the microsphere surface. A shift in the resonance frequency signals the binding event (a.k.a. hybridization).

Suppose a strand of DNA (a.k.a. as an oligonucleotide, abbrev. oligo), which we will call the target, contains 11 bases that spell out the nonsensical word GATAGAGTCAG. The compliment is. CTATCTCAGTC. A change in the compliment in the 5th letter from the left from C to A is clearly a defect in relation to the target. We would like to design a way to use our photonic atom biosensor in order detect this defect. Since one molecular defect out of eleven bases is a small difference, the target could partially bind to the defective strand. A means for discriminating this imposter from the real thing has to be invented. The solution takes advantage of the frequency domain nature of our photonic atom sensor.

Since it would be extremely difficult to generate two high Q spheres which would have the same resonance spectra,¹⁷ each sphere is distinguishable by its resonant frequency. So the resonant frequency marks the microsphere and locates it in the frequency domain. Attaching a particular word of DNA to a given sphere locates that DNA in frequency space. If we mark one sphere (call it S1) with many duplicates of CTATCTCAGTC and another S2 with duplicates of CTATATCAGTC, then a target GATAGAGTCAG should seek out the sphere S1 preferentially. The implementation of this idea fits beautifully into the fiber-sphere coupling scheme since the spectrum taken through the fiber should reveal each sphere separately, and two spheres sitting on the same fiber can be bathed simultaneously in a sample of stirred fluid containing the target (i.e. similar to the cell in Fig.2, but with two spheres). Then it is only a matter of tracking the shift in the resonant dips from each as the target is adsorbed. This basic idea is depicted by the cartoon in Fig.10.

Of course, there are many details to making the Photonic Atom SNP Detector a reality. For one thing one has to functionalize the silica surface of the microsphere to adsorb the oligos of DNA. To do this Frank Vollmer attached a biotinylated dextran polymer to the silica surfaces of S1 and S2, and allowed both to be reacted with streptavidin.¹⁴ Since streptavidin has four sites for attaching biotin (Fig.8) three sites remained for adding biotinylated-DNA. Of course, these DNA additions must be done separately in order that S1 is covered with CTATCTCAGTC and S2 with CTATATCAGTC. In addition there is a primary physical effect that must be verified.

The physical effect has to do with the independence with which the resonators can be stimulated. The approach to checking this is to first place one sphere in contact with the fiber and observe the spectrum. After this the other makes contact. Fig.11 shows the way in which the spectra are changed. So long as the surface of the spheres are separated by more than ~200 nm there is no apparent interaction. The resonances which appear after the first sphere touches the fiber are preserved upon contact with the second sphere. The second sphere, however, contributes its own resonances to the spectrum, as our frequency domain argument anticipated.

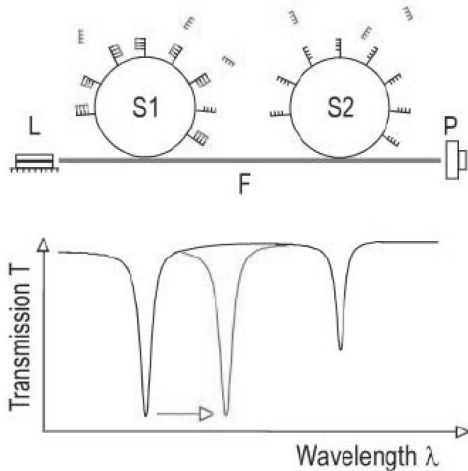


Fig.10 Two microspheres touching the same fiber and having separate words of DNA are bathed in fluid containing a target. If the SNP sensing idea is correct then the sphere containing the compliment to the target should preferentially shift its resonance (cartoon: lower figure).

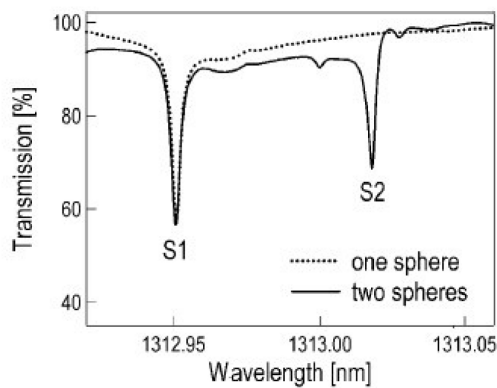


Fig.11 The spectrum after one sphere contacts an eroded optical fiber about $4\mu\text{m}$ in diameter (solid line), and when both spheres are in contact (dotted line).¹⁵

The results of the SNP experiment are shown in Fig.12A. As the target is injected into the cell the frequencies of the resonances associated with microspheres S1 and S2 begin to change. Both show jagged fluctuations in the frequencies of approximately equal intensity. These fluctuations are apparently due to the pipetting process in which $10\mu\text{l}$ of the target solution is injected into the 1 ml cell containing a buffer solution. Following these fluctuations the wavelength of the resonance associated with S1 shows a systematic red shift. Microsphere S2 shows a substantially smaller shift (less than one sixth).

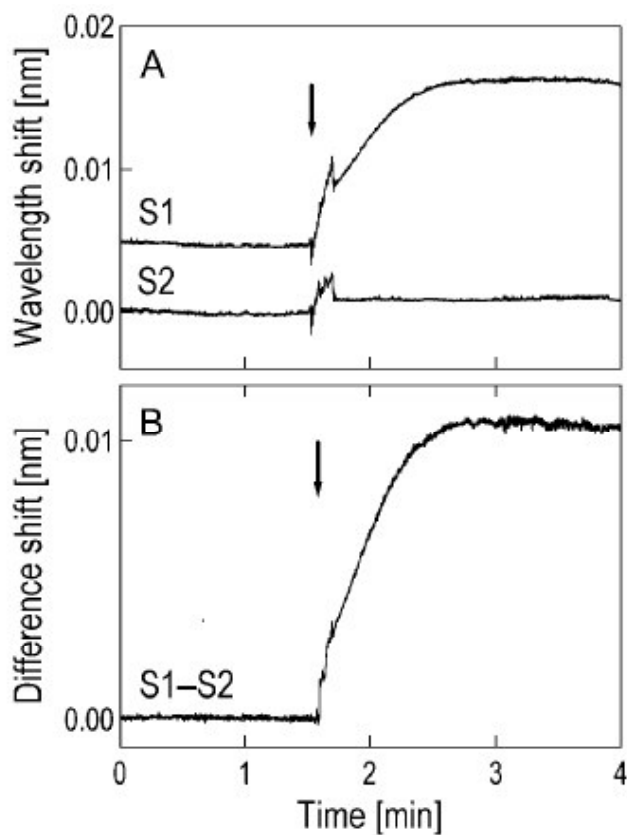


Fig.12A Shift of resonances of spheres S1 and S2 following target injection. 12B Differential shift, $(\delta\lambda)_{S1} - (\delta\lambda)_{S2}$.¹⁵

The original fluctuations may be considered as a common mode noise similar to the sort of noise that enters the inputs of a differential amplifier. If so a simple subtraction between the shifts associated with the S1 signal and the S2 signal should cancel this common mode noise. Fig.12B shows this differential signal. Here we see the real time discrimination of one letter of DNA with a very large signal-to-noise ratio, 54!

9. Future Directions

By reducing the microsphere radius our sensitivity will increase⁴ allowing us to see smaller and smaller fractions of a monolayer, until we may ultimately reach a single bio-particle. At this point it may be possible to count label-free molecules one at a time rather than wait for a full monolayer to form. Each step in increased wavelength will be directly proportional to the polarizability α and therefore to the molecular weight. It may be unnecessary for molecules to land on the surface. If they simply flow through the evanescent field of a mode, then the frequency shift will pulse, and molecular counting and analysis becomes possible. Of course, there are noise problems associated with this idea. The molecules are under intense Brownian forces. The Brownian noise interval will be severely reduced if the molecule is carried by a flow. Here we require a flow system, in the form of a micro-fluidic channel.

At the same time as the flow system is assembled our tapered and tenuous fiber waveguide must be replaced with something more robust. Instead of employing lithography and micro-manufacturing techniques¹⁸ we favor supporting the tapered fiber with a substrate. In contrast to the aerogel supports demonstrated by the Mazur group for supporting nano-fibers,¹⁹ we favor a less porous material with the refractive index of water. Recent work at the Polytechnic²⁰ and elsewhere on fluoro-polymers, have show that this moldable material is essentially non-porous, as robust as plexiglass (i.e. PMMA), and has the refractive index of water.

Fig.13 shows the micro-fluidic concept,²¹

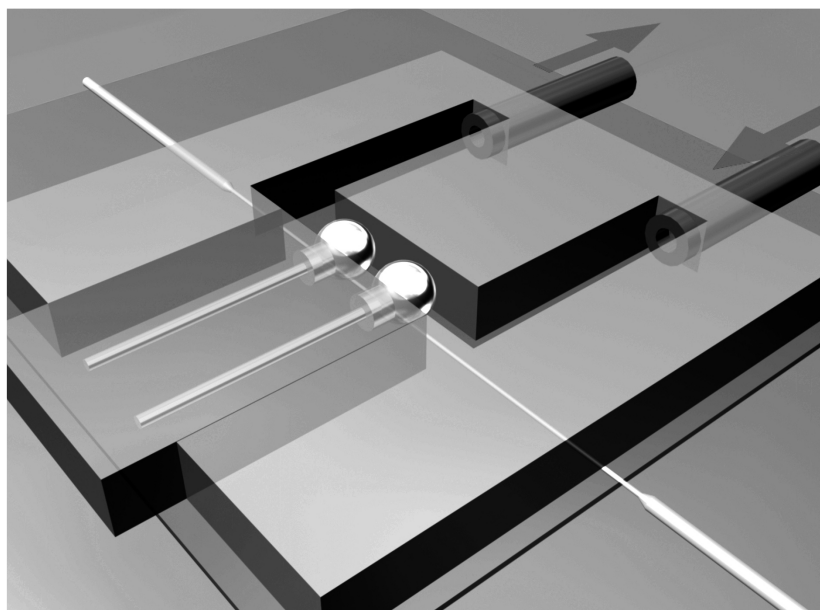


Fig.13 Dual-sphere sensor consists of micro-fluidic channel with tapered fiber sandwiched between two layers of fluoro-polymer. Spheres are mounted on a polymer cassette while coupled to the fiber. Flow passes from right to left

Acknowledgements

Steve Arnold thanks Rino DiBartolo for his kind invitation to lecture at this school and for once again introducing him to the land of Rino's birth.

This was the third time Steve attempted to make a course out of his research. By learning from those who have done this in the past years, he gained a great deal of insight into the technique. Steve is particular indebted to Eric Mazur and Ralph von Baltz for their encouragement.

Without the prodding and encouragement from Ottavio Forte this manuscript would not have been completed on time. Bravo Ottavio.

Both of us would like to thank the Othmer Institute for Interdisciplinary Studies at the Polytechnic, and the NSF (BES Grant No. 0522668) for support.

References

1. P. N. Prasad, *Introduction to Biophotonics* (Wiley-Interscience, New Jersey, 2003).
2. A. Serpenguzel, S. Arnold, and G. Griffel, "Excitation of resonances of microsphere on an optical fiber", *Opt. Lett.* **20**, 654-656 (1995).
3. S. Arnold, "Microspheres, Photonic Atoms, and the Physics of Nothing", *American Scientist* **89**, 414-421 (2001).
4. S. Arnold, M. Khoshima, I. Teraoka, S. Holler, and F. Vollmer, "Shift of whispering gallery modes in microspheres by protein adsorption", *Opt.Lett.* **28**, 272(2003).
5. J.C. Knight, G. Cheung, F. Jacques, and T.A. Birks, "Phase-matched excitation of whispering-gallery-mode resonances by a fiber taper," *Opt.Lett.* **22**, 1129(1997).
6. M.L. Gorodetsky, A.A. Savchenkov, and V.S. Ilchenko, "Ultimate Q of optical microsphere resonators," *Opt.Lett.* **21**, 453(1996).
7. S. Arnold, M. Noto, and F. Vollmer, "Consequences of extreme photon confinement in micro-cavities: I. ultra-sensitive detection of perturbations by bio-molecules," in *Frontiers of optical spectroscopy: investigating extreme physical condition with advanced optical techniques*, Ed. Baldassare DiBartolo (Kluwer Publishers, 2005)
8. S. Arnold, and S. Holler, "Microparticle photophysics: Fluorescence microscopy and spectroscopy of a photonic atom," in *Cavity-enhanced spectroscopies*, R D. van Zee, and J. P. Looney, eds. (Academic, San Diego, Calif., 2002), pp. 227-253
9. E. S. C. Ching, P. T. Leung, and K. Young, "Optical processes in microcavities-the role of quasinormal modes," in *Optical process in microcavity*, R. K. Chang, and A. J. Campillo, eds. (World Scientific, Singapore, 1996), pp. 1-76.
10. M. Noto, F. Vollmer, D. Keng, I. Teraoka, and S. Arnold, "Nanolayer Characterization through Wavelength Multiplexing a Microsphere Resonator", *Opt.Lett.* **30**, 510-512(2005).
11. J. P Laine, B. E. Little, and H. A. Haus, "Etch-eroded fiber coupler for whispering-gallery-mode excitation in high-Q silica microspheres," *IEEE Photon. Tech. Lett.* **11**, 1429-1430 (1999).
12. F. Vollmer, D. Braun, A. Libchaber, M. Khoshsima, I. Teraoka, and S. Arnold, "Protein detection by optical shift of a resonant microcavity," *Appl. Phys. Lett.* **80**, 4057-4059 (2002).
13. I.N. Levine, *Physical Chemistry*, 4th Ed., (McGrew-Hill, INC., New York, 1995), p.366.
14. M. Noto, M. Khoshsima, D. Keng, I. Teraoka, V. Kolchenko and S. Arnold, "Molecular weight dependence of a whispering gallery mode biosensor" *Appl.Phys.Lett.* (in press, 2006).
15. F. Vollmer, S. Arnold, D. Braun, I. Teraoka, and A. Libchaber, "Multiplexed DNA Quantification by Spectroscopic Shift of Two Microsphere Cavities", *Biophysical Journal* **85**, 1974-1979(2003).
16. D. Watson and F. H. Crick, "Molecular structure of Nucleic Acids" *Nature* **171**, 737-738(1953).

-
17. With a Q of 10^7 , attempting to make two spheres spectrally the same over even 1 resonant width would require a tolerance in the equatorial radius of better than 1 part in 10^7 which for a $100\mu\text{m}$ radius is 0.01nm !
 18. BE Little, JP Laine, DR Lim, HA Haus, and LC Kimerling, and S.T. Chu, *Opt.Lett.***25** 73(2000).
 19. L. Tong, J. Lou, R.R. Gattass, S. He, X. Chen, L. Liu, and E. Mazur, "Assembly of Silica Nanowires on Silica Aerogels for Microphotonic Devices" *Nano Lett.***5**, 259-262(2005).
 20. F. Mikes, Y. Yang, I. Teraoka, T. Ishigure, Y. Koike, and Y. Okamoto,"Synthesis and Characterization of an Amorphous Perfluoropolymer: Poly(perfluoro-2-methylene-4-methyl-1,3-dioxolane)", *Macromolecules* **38**, 4237-4245(2005).
 21. O. Gaathon, W. Jeck, I. Teraoka, and S. Arnold (in progress).